

Cluster-based network modeling—automated robust modeling of complex dynamical systems

Daniel Fernex,¹ Bernd R. Noack², Richard Semaan^{1*}

¹Institut für Strömungsmechanik, Technische Universität Braunschweig,
Hermann-Blenk-Str. 37, 38108 Braunschweig, Germany

²Center for Turbulence Control, Harbin Institute of Technology,
Shenzhen 518058, People’s Republic of China

*To whom correspondence should be addressed; E-mail: r.semaan@tu-braunschweig.de.

We propose a universal method for data-driven modeling of complex nonlinear dynamics from time-resolved snapshot data without prior knowledge. Complex nonlinear dynamics govern many fields of science and engineering. Data-driven dynamic modeling often assumes a low-dimensional subspace or manifold for the state. We liberate ourselves from this assumption by proposing cluster-based network modeling (CNM) bridging machine learning, network science, and statistical physics. CNM only assumes smoothness of the dynamics in the state space, robustly describes short- and long-term behavior and is fully automatable as it does not rely on application-specific knowledge. CNM is demonstrated for the Lorenz attractor, ECG heartbeat signals, Kolmogorov flow, and a high-dimensional actuated turbulent boundary layer. Even the notoriously difficult modeling benchmark of rare events in the Kolmogorov flow is solved. This automatable universal data-driven representation of complex nonlinear dynamics complements and expands network connectivity science and promises new fast-track avenues to understand, estimate, predict and control complex systems in all scientific fields.

1 Introduction

Climate, epidemiology, brain activity, financial markets and turbulence constitute examples of complex systems. They are characterized by a large range of time and spatial scales, intrinsic high dimensionality and nonlinear dynamics. Dynamic modeling for the long-term features is a key enabler for understanding, state estimation from limited sensors signals, prediction, control, and optimization. Data-driven modeling has made tremendous progress in the last

decades, driven by algorithmic advances, accessibility to large data, and hardware speedups. Typically, the modeling is based on a low-dimensional approximation of the state and system identification in that approximation.

The low dimensional approximation may be achieved with subspace modeling methods, such as proper orthogonal decomposition (POD) models [1, 2], dynamic mode decomposition (DMD) [3] and empirical dynamical modeling [4], to name only a few. Autoencoders [5] represent a general nonlinear dimension reduction to a low-dimensional feature space. The dynamic system identification is significantly simplified in this feature space.

An early breakthrough in system identification was reported by Bongard and Lipson [6] using symbolic regression. The method performs a heuristic search of the best equation that describes the dynamics [7]. They are however expensive and not easily scalable to large systems. Recent developments in parsimonious modeling lead to the “sparse identification of nonlinear dynamics” (SINDy) algorithm that identifies accurate parsimonious models from data [8]. Similarly, SINDy is not easily scalable to large problems. The computational expense becomes exorbitant already for moderate dimensional feature spaces.

This limitation may be by-passed by black-box techniques. These include Volterra series [9], autoregressive models [10] (e.g., ARX, ARMA, and NARMAX), eigensystem realization algorithm (ERA) [11], and neural network (NN) models [12]. These approaches, however, have limited interpretability and provide little physical insights. Some (e.g. NN) require large volumes of data and long training time, luxuries that are not always at hand.

In this study, we follow a novel modeling paradigm starting with a time-resolved snapshot set. We only assume smoothness of the dynamics in the state space liberating ourselves from the requirement of a low-dimensional subspace or manifold for the data and analytical simplicity of the dynamical system. The snapshots are coarse-grained into a small number of centroids with clustering. The dynamics is described by a network model with continuous transitions between the centroids. The resulting cluster-based network modeling (CNM) uses time-delay embedding to identify models with an arbitrary degree of complexity and nonlinearity. The methodology is developed within the network science [13, 14, 15] and statistical physics [16] frameworks. Due to its generic nature, network analysis is being increasingly used to investigate complex systems [17, 18]. The proposed method builds on previous work by Kaiser et al. [19], where clustering is used to coarse-grain the data into representative states and the temporal evolution is modeled as a probabilistic Markov model. By construction, the state vector of cluster probabilities converges to a fixed point representing the post-transient attractor, i.e., the dynamics disappear. A recent improvement [20] models the transition dynamics between the network nodes as straight constant-velocity ‘flights’ with a travel time directly inferred from the data. The present study expands on these innovations and generalizes the approach to arbitrary high-order chains with time-delay coordinates [21], and introduces a control-oriented extension to include external inputs and control. Besides its accuracy, one major advantage the method has is the ability to control the resolution level through adaptive coarse-graining.

Dynamics of complex systems is often driven by complicated small-scale (sometimes microscopic) interactions (e.g. turbulence, biological signaling) that are either unknown or very

expensive to fully-resolve [22]. The resolution of cluster-based network modeling can be adapted to match any desired level, even when microscopic details are not known. This universal representation of strongly nonlinear dynamics, enabled by adaptive coarse-graining and a probabilistic foundation, promises to revolutionize our ability to understand, estimate, predict and control complex systems in all scientific fields. The method is inherently robust and honest to the data. It requires no assumption on the analytical structure of the model, and is computationally tractable, even for high-degrees of freedom problems. A code is available at: <https://github.com/fernexda/cnm>.

2 Cluster-based network modeling

Robust probability-based data-driven dynamical modeling for complex nonlinear systems has the potential to revolutionize our ability to predict and control these systems. Cluster-based network models (CNM) reproduce the dynamics on a directed network, where the nodes are the coarse-grained states of the system. The transition properties between the nodes are based on high-order direct transition probabilities identified from the data. The model methodology is applied to a variety of dynamical systems, from canonical problems such as the Lorenz attractor to rare events to high degrees of freedom systems such as a boundary layer flow simulation. The general methodology is illustrated in Fig. 1 with the Lorenz system and is detailed in the following.

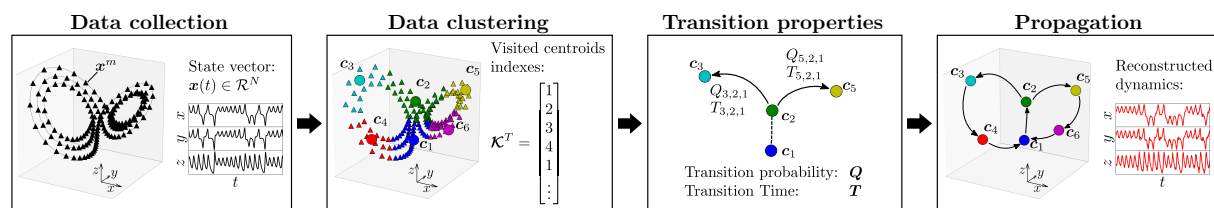


Fig. 1. Cluster-based network modeling methodology. M consecutive N -dimensional states $x(t) \in \mathcal{R}^{N \times M}$ are collected at fixed sampling frequency. Based on their similarity, the states are grouped into K clusters. The network nodes are computed as the cluster centroids c_i , and the transition time T and transition probability Q between the nodes are identified from the data. The CNM dynamics are propagated as consecutive flights between centroids. Each transition is characterized by its destination, given by Q , and its transit time given by T .

Data collection and clustering. The starting point of CNM is the data collection of M consecutive discrete N -dimensional state of the system $x(t) \in \mathcal{R}^N$ equally-spaced in time with Δt , such that the state at t^m is $x(t^m) = x(m\Delta t) = [x_1^m, \dots, x_N^m]$. The discrete states are grouped into K clusters \mathcal{C}_k and the network nodes are identified as the clusters' centroids c_k , defined as the average of the states in each cluster. In this study, clustering is achieved with the

unsupervised k -means++ algorithm [23, 24] that minimizes the inner-cluster variance. Other clustering algorithms are possible. The choice is a problem-dependent option. The vector $\mathcal{K} = [\mathcal{K}_1, \dots, \mathcal{K}_I]$, $\mathcal{K}_i \in [1, K]$, contains the indexes of the consecutively-visited clusters over the entire time sequence, such that \mathcal{K}_i is the index of the i th visited cluster. The first and last clusters are $\mathcal{C}_{\mathcal{K}_1}$ and $\mathcal{C}_{\mathcal{K}_I}$, respectively. The size I of \mathcal{K} is equal to the number of transitions between K centroids over the entire ensemble plus one. We note that two sequential cluster visits are not necessarily equally-spaced in time, but rather depend on the state's rate of change in their vicinity.

Transition properties. Before we detail the transition properties of cluster-based network models [20], we briefly review those of cluster-based Markov models [19] upon which the current method builds. In cluster-based Markov models, the state variable is the cluster population $\mathbf{p} = [p_1, \dots, p_K]^T$, where p_i represents the probability to be in cluster i and the superscript T denotes the transpose. The transitions between clusters are modeled with a first-order Markov model. The probability to move from cluster \mathcal{C}_j to cluster \mathcal{C}_k is described by the transition matrix $\mathbf{P} = (P_{k,j}) \in \mathcal{R}^{K \times K}$ as

$$P_{k,j} = \Pr(\mathcal{K}_i = k | \mathcal{K}_{i-1} = j). \quad (1)$$

The transition matrix \mathbf{P} is computed as

$$P_{k,j} = \frac{n_{k,j}}{n_j}, \quad (2)$$

where $n_{k,j}$ are the number of samples that move from \mathcal{C}_j to \mathcal{C}_k , and n_j is the number of transitions departing from \mathcal{C}_j regardless of the destination point.

In [19], the transition time Δt is a user-specified constant. Let \mathbf{p}^l be the probability vector at time $t^l = l\Delta t$, then the change in one time step is described by

$$\mathbf{p}^{l+1} = \mathbf{P} \mathbf{p}^l. \quad (3)$$

With time evolution, equation (3) converges to the asymptotic probability $\mathbf{p}^\infty := \lim_{l \rightarrow \infty} \mathbf{p}^l$. In a typical case, equation (3) has a single fixed point \mathbf{p}^∞ .

Conversely, CNM relies on the *direct transition matrix* \mathbf{Q} , which ignores inner-cluster residence probability and only considers inter-cluster transitions. The direct transition probability is inferred from data as

$$Q_{k,j} = \frac{n_{k,j}}{n_j}, \quad (4)$$

with $Q_{j,j} = \Pr(\mathcal{K}_i = j | \mathcal{K}_{i-1} = j) = 0$, by the very definition of a direct transition. Generalizing to an L -order model, which is equivalent to using time-delay coordinates, the direct transition probability is expressed as $\Pr(\mathcal{K}_i | \mathcal{K}_{i-1}, \dots, \mathcal{K}_{i-L})$. Illustrating for a second-order model the probability to move to \mathcal{C}_l having previously visited \mathcal{C}_k and \mathcal{C}_j is given by

$$Q_{l,k,j} = \Pr(\mathcal{K}_i = l | \mathcal{K}_{i-1} = k, \mathcal{K}_{i-2} = j). \quad (5)$$

Time-delay embedding is a cornerstone of dynamical systems [25]. The optimal Markov chain order L is problem-dependent (see Appendix D). Larger L values are typically necessary for problems with complex phase-space trajectories. In this study, we shall demonstrate how time-delay embedding benefits extend to higher-order cluster-based network models.

The second transition property is the transition time. For Markov models, the time step is a critical user-defined design parameter. If the time step is too small, the cluster-based Markov model idles many times in each cluster for a stochastic number of times before transitioning to the next cluster. The model-based transition time may thus significantly deviate from the deterministic data-driven trajectories through the clusters. If the time step is too large, one may miss intermediate clusters. This design parameter can be avoided in cluster-based network modeling (CNM). The key idea is to abandon the ‘stroboscopic’ view and focus on non-trivial transitions, thus avoiding rapid state diffusion. Let t^n and t^{n+1} be the time of the first and last snapshots to enter and, respectively, to leave \mathcal{C}_k at the n th iteration (Fig. 2). Here, iterations refer

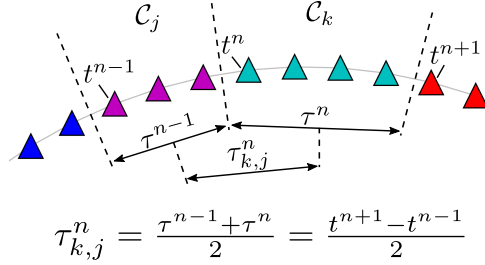


Fig. 2. Definition of the transition time between clusters \mathcal{C}_j and \mathcal{C}_k . The transit time τ^n in \mathcal{C}_k at iteration n is the time range spanned by the data entry and exit times in the clusters, t^n and t^{n+1} . The individual transition time $\tau_{k,j}^n$ is defined as the average transit time between two neighboring clusters.

to the sequential jumps between the centroids. The residence time $\tau^n = t^{n+1} - t^n$ corresponds to the duration of the state transit in cluster \mathcal{C}_k at this iteration. We define the individual transition time from cluster j to cluster k for one iteration as half the residence time of both clusters,

$$\tau_{k,j}^n = \frac{\tau^{n-1} + \tau^n}{2} = \frac{t^{n+1} - t^{n-1}}{2}. \quad (6)$$

Averaging all $n_{k,j}$ individual transition times between \mathcal{C}_j to \mathcal{C}_k yields the transition time $T_{k,j} = 1/n_{k,j} \sum_{n=1}^{n_{k,j}} \tau_{k,j}^n$. This definition may appear arbitrary but is the least-biased guess consistent with the available data. Similar to the direct transition matrix \mathbf{Q} for an L -order chain, the transition time matrix $\mathbf{T} = (T_{k,j}) \in \mathcal{R}^{K \times K}$ also depends on the $L - 1$ previously visited centroids. When L is large, this could yield to two storage-intensive $L + 1$ -dimensional tensors \mathbf{Q} and \mathbf{T} with K^{L+1} elements. The expensive tensor creation and storage is circumvented by a lookup table (LUT), where only non-zero entries that correspond to actual transitions are retained. The look-up tables are typically orders-of-magnitude smaller than the full tensors. (see Appendix B).

Propagation. The final step in cluster-based network modeling propagates the state motion. We assume a uniform state propagation between two centroids \mathbf{c}_j and \mathbf{c}_k as,

$$\mathbf{x}(t) = \alpha_{kj}(t)\mathbf{c}_k + [1 - \alpha_{kj}(t)]\mathbf{c}_j, \quad \alpha_{kj} = \frac{t_j - t}{T_{k,j}}, \quad (7)$$

where t_j is the time when the centroids \mathbf{c}_j is left. The motion between the centroids may be interpolated with splines for smoother trajectories. As CNM is purely data-driven, the model quality is directly related to that of the training data. More specifically, the sampling frequency and total time range must be selected, such that all relevant dynamics are captured and are statistically fully converged. This usually requires a larger amount of data than other data-driven methods, such as ARMA and SINDy.

3 Results

CNM of the Lorenz system. CNM is applied to the Lorenz system, a widely-used canonical chaotic dynamical system [26] defined by three coupled nonlinear differential equations,

$$\begin{aligned} \frac{dx}{dt} &= \sigma(y - x) \\ \frac{dy}{dt} &= x(\rho - z) - y \\ \frac{dz}{dt} &= xy - \beta z, \end{aligned} \quad (8)$$

where the system parameters are here defined as $\sigma = 10$, $\rho = 28$ and $\beta = 8/3$. The data are clustered with $K = 50$ centroids, depicted in Fig. 3A. The snapshots are colored based on their cluster affiliations. CNM is performed with a chain order $L = 22$ using ≈ 17000 transitions, which cover the same time range as that of the original data. The optimal K and L values are problem-dependent. They are identified for the Lorenz system through a parametric study, where the root-mean square error of the autocorrelation function between the reference data and the model is minimized (c.f. Appendix D).

Time series obtained with CNM agree very well with the reference data (Fig. 3B and C). The oscillating amplitude growth in both ears, as well as the ear switching, are correctly captured. The cluster probability distribution (CPD) q_k , $k = 1, \dots, K$ provides the probability of the state to be in a specific cluster. It indicates whether the modeled trajectories populate the phase space similarly to the reference data (c.f. Appendix C). The CPD for both the data and CNM is shown in Fig. 3D. For clarity, q_k is shown with 10 clusters only instead of the full 50 clusters. As the figure shows, CNM accurately reproduces the probability distribution. Following Protas et al. [27], the cluster-based network model is validated based on the autocorrelation function of the state vector. This function avoids the problem of comparing two trajectories with finite dynamic prediction horizons due to phase mismatch. The autocorrelation function also yields

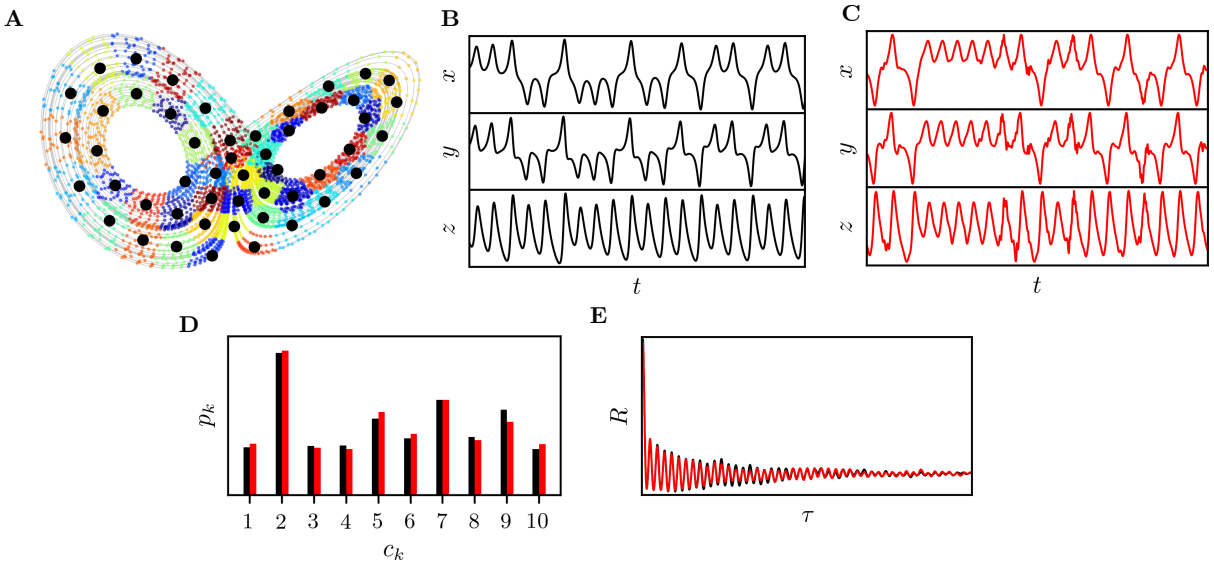


Fig. 3. Cluster-based network modeling of the Lorenz system. (A) Phase-space representation of the data clustering. The centroids are depicted with black circles and the small circles are the snapshots, colored by their cluster affiliation. The CNM accuracy is demonstrated in the accurate reproduction of (B)-(C) the time series, (D) the cluster probability distribution, and (E) the autocorrelation function. Black and red coloring denotes the reference and CNM data, respectively.

the fluctuation energy at vanishing delay $R(0)$ and can be used to infer the spectral behavior (see Appendix C). As Fig. 3E shows, CNM accurately reproduces the fast oscillatory decay, even after dozens of oscillations, as well as the fluctuation energy $R(0)$, which is reproduced with a 2.8% rms error. This performance is in contrast to the cluster-based Markov models, where time integration leads to the average flow, and to first-order cluster-based network models [20], where the prediction accuracy is significantly lower. A detailed comparison between the cluster-based Markov model, the first-order cluster-based network model, and the current model is provided in Appendix E.

Demonstration on examples. Cluster-based network modeling is applied to numerous examples, ranging from analytical systems to real-life problems using experimental and simulation data. The main results are summarized in Fig. 4. Details on each application are provided in Appendix A. The first two applications are the Lorenz [26] and Rössler [28] attractors, typical candidates for dynamical systems analysis. The two systems are governed by simple equations and exhibit chaotic behavior under specific parameter values. The following two implementations are one-dimensional systems: electrocardiogram measurements (ECG) [29], and the dissipative energy from a Kolmogorov flow [30]. Whereas the ECG exhibits the regular heart-beat pattern, the dissipative energy of the Kolmogorov flow is quasi-random with intermittent bursts. The last CNM application is a high-dimensional large eddy simulation of an actuated turbulent boundary layer for skin friction reduction [31]. The clustering step on this ≈ 5 million grid cells simulation is performed on the mode coefficients of a lossless proper orthogonal decomposition. This dimensionality reduction step significantly reduces the computational load while yielding the same clustering outcome as the full difference matrix [19]. The boundary layer time series are therefore represented with the mode coefficients.

In each example, both the qualitative and quantitative dynamics are faithfully captured. The reconstructed time series are hardly distinguishable from the original data. Intermittent events such as the peaks in the Rössler z -component and the dissipation energy bursts of the Kolmogorov flow are statistically very well reproduced. The autocorrelation distributions of both reference data and models match perfectly over the entire range, demonstrating both robustness and accuracy. We note that robustness is inherent to CNM, since the modeled state always remains close to the training data.

The CPD of the data and CNM for the Rössler system, the ECG signal, the Kolmogorov flow dissipation energy and the actuated turbulent boundary layer are presented in Fig. 5. For all cases, CNM accurately reconstructs the distributions. Remarkably, the probabilities of less visited-clusters corresponding to rare events for the Kolmogorov flow (Fig. 5C) or fast events such as the peaks in the z directions of the Rössler attractor (Fig. 5A) and the heartbeat pulse (Fig. 5B) are very well captured by CNM.

A special characteristic of CNM is its ability to accurately model and predict systems with rare events. This ability is rooted in the probabilistic framework upon which CNM is constructed, where the recurrence properties are the same as the reference data. If one cluster is visited multiple times (or seldom) in the data, it will also be a recurrence point of the CNM.

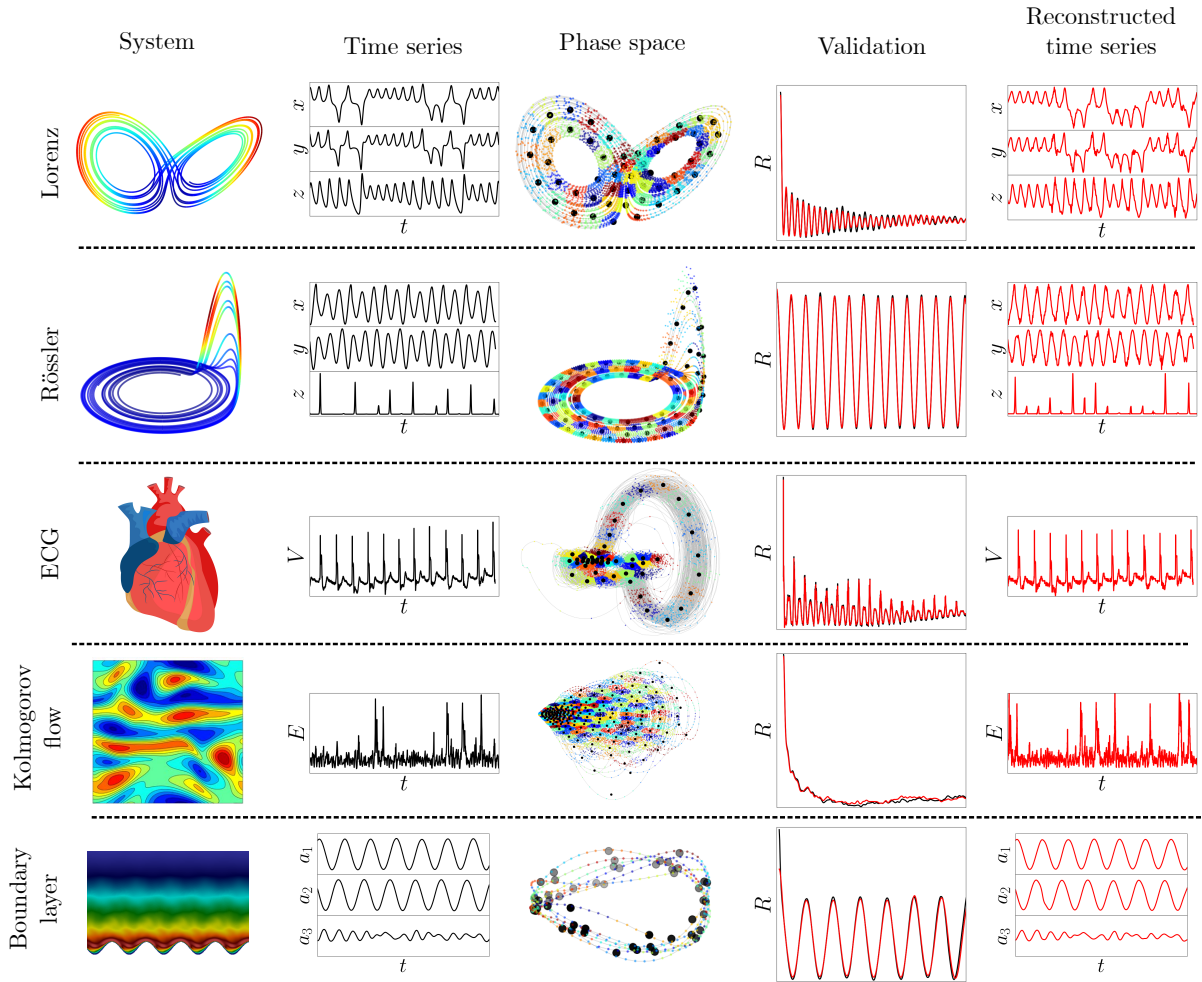


Fig. 4. The cluster-based network modeling implemented on five applications covering a wide range of dynamics. The first two applications are three-dimensional chaotic systems, the Lorenz and Rössler attractors. The two following examples are one-dimensional experimental measurements from an electrocardiogram and numerical simulation of the dissipation energy in a Kolmogorov flow. The final application is a large-eddy simulation of an actuated turbulent boundary layer. The excellent match of the autocorrelation functions for all applications demonstrate the CNM’s ability to capture the relevant dynamics for any complex nonlinear system. The modeled time series faithfully reconstruct the data including the intermittent quasi-random bursts of the Kolmogorov dissipation energy, as well as the z -component pulses of the Rössler system.

A generic example of a rare events problem is the Kolmogorov flow [32], a two-dimensional

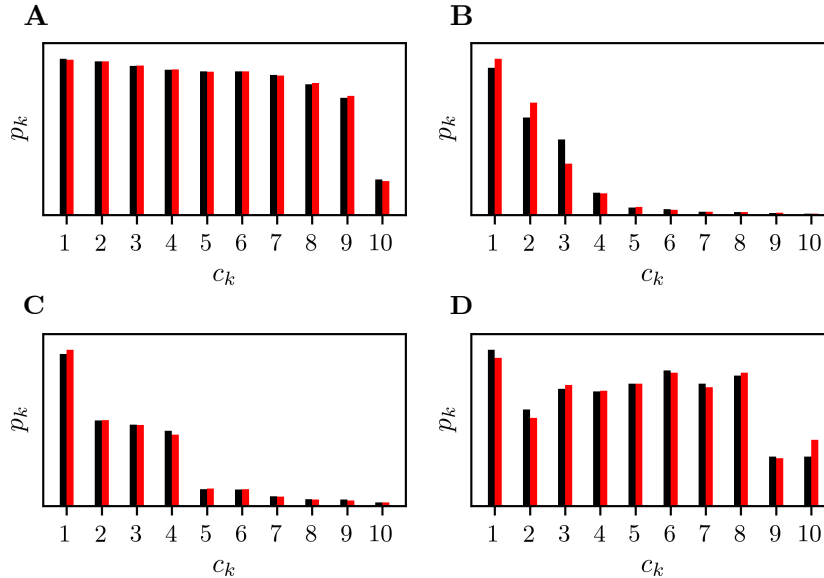


Fig. 5. Cluster probability distribution (CPD) of the data and CNM for four applications. (A)-(D) CPD of the Rössler system, ECG signal, Kolmogorov flow dissipation energy, and actuated turbulent boundary layer, respectively. For all cases, the data (black) and CNM (red) are in good agreement. The specific features of each dataset, such as the rare events of the Kolmogorov dissipation energy and the fast heartbeat pulses are probabilistically well reconstructed by CNM.

incompressible flow with sinusoidal forcing. With a sufficiently high forcing wavenumber, the flow becomes unstable and the dissipation energy D exhibits intermittent and spontaneous bursts (c.f. Fig. 6A). The dashed line denotes an arbitrary threshold beyond which a peak is considered a rare event. The probability distribution function (PDF) of the dissipation energy from the data and CNM are compared in Fig. 6B. The main peak centered around zero reflect the stochastic nature of the dissipation energy, whereas the tail depicts rare events whose occurrence probability decreases with their amplitude. As the figure shows, CNM accurately captures the probabilistic behavior of the dissipation energy. Both the main stochastic peak and the rare event tail of the distribution are well reproduced. Moreover, the total number of bursts in the current sequence is well reproduced, with 58 bursts in the original data compared to 62 for CNM.

Control-oriented cluster-based network modeling (CNMc). To disambiguate the effect of internal dynamics from actuation or external input, we generalize CNM to include control \mathbf{b} . The transition probabilities $Q(\mathbf{b})$ and transition times $T(\mathbf{b})$ are first identified for each actuation setting \mathbf{b} individually. The three-step procedure for the propagation of a new control command $\hat{\mathbf{b}}$ depicted in Fig. 7A is then performed. At each iteration, (1) a search for the nearest cen-

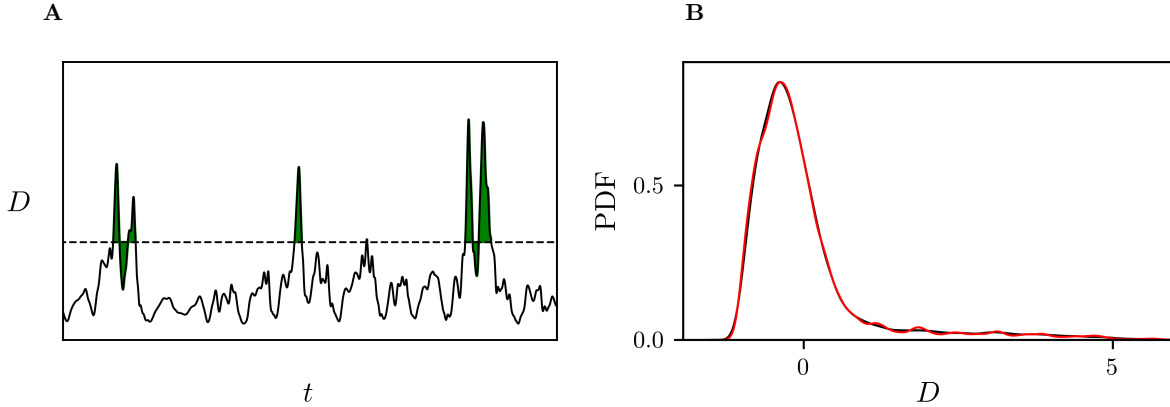


Fig. 6. Rare events from the Kolmogorov flow dissipation energy. (A) Time series of the dissipation energy D . The dashed line denotes an arbitrary threshold beyond which the peaks, represented with green filling, are considered a burst. (B) Probability distribution of the data (black) and CNM (red). Both the main peak and the decaying tail of the distribution are accurately reproduced.

troids from the two closest actuation test cases is performed. (2) Their transition properties are then identified and (3) averaged to determine the transition of the state \hat{x} . More details of the CNMc algorithm are provided in Appendix F. CNMc is applied to two systems at new control conditions, the Lorenz attractor and the actuated turbulent boundary layer. The Lorenz system with $\rho = 28$ is interpolated from two test cases with $\rho = 26$ and $\rho = 30$ and the boundary layer with actuation parameters $\lambda^+ = 1000$, $T^+ = 120$ and $A^+ = 30$ is interpolated from cases with $\lambda^+ = 1000$, $T^+ = 120$, $A^+ = 20$ and $\lambda^+ = 1000$, $T^+ = 120$, $A^+ = 40$. The CNMc settings are listed in Table 3. Despite the algorithm’s simplicity, the main dynamics are properly captured, as shown by the autocorrelation functions in Fig. 7B and 7C, and the time series (Fig. 14). CNMc is cast in the same probabilistic framework as CNM and thereby retains all previously-demonstrated advantages. As the dynamics are interpolated from centroids that belong to potentially different trajectories, the resulting motion might be noisier and a larger number of centroids than regular CNM are typically required.

4 Discussion

We propose a universal data-driven methodology for modeling nonlinear dynamical systems. The method builds on prior work in cluster-based Markov modeling and network dynamics. Cluster-based network modeling has several unique and desirable features. (1) It is simple and automatable. Once the various schemes are chosen (e.g., clustering algorithm, transition time, etc), only two parameters must be selected: the number of clusters K and the Markov chain order L . Too few centroids might oversimplify the dynamics, whereas too many might

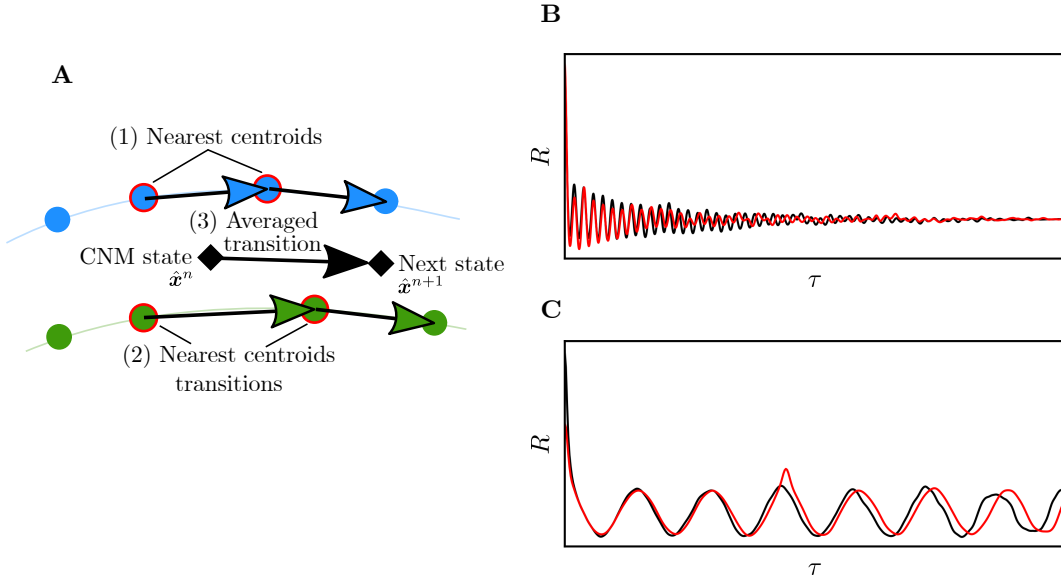


Fig. 7. Control-oriented cluster-based network modeling (CNMc). (A) CNMc iteratively propagates the state in the phase-space populated with the centroids from the two operating conditions with the closest control parameters. (1) Neighboring centroids to the current state $\hat{\mathbf{x}}^n$ at iteration n are first identified. (2) Their transition properties are calculated and then (3) averaged to determine the next state $\hat{\mathbf{x}}^{n+1}$. CNMc accuracy is demonstrated by the autocorrelation function distributions of the data (black) and the predicted case (red) for the (B) Lorenz system and the (C) actuated turbulent boundary layer, respectively.

lead to a noisy solution. We note that a high Markov chain order L is not always necessarily advantageous. Both parameters are problem-dependent and can be automatically optimized. (2) The method does not require any assumption on the analytical structure of the model, only some sense of smoothness. It is always honest to the data. (3) The offline computational load is low. In fact, the most expensive step in the process is the occasionally-required snapshot-based proper-orthogonal decomposition (POD) for dimensionality reduction. After the POD computation, the clustering and network modeling require a tiny fraction of the computational operation. (4) The recurrence properties are the same as the reference data. If one cluster is visited multiple times (or seldom) in the data, it will also be a recurrence point of the CNM. This feature is what enables modeling of problems with rare events. (5) Long-term integration will never lead to divergence – unlike, e.g., POD-based models. The simplicity and robustness, however, have a price. On the kinematic side, the simple CNM version cannot extrapolate, e.g., resolve oscillations at higher amplitudes not contained in the data. On the dynamic side, we lose the relationship to first principles: The network model is purely inferred from data, without links to the governing equations. In particular, cluster-based models are not natural frameworks for dynamic instabilities, as the notion of exponential growth and nonlinear saturation is intimately

tied to Galerkin expansions. Subsequent generalizations need to overcome these restrictions. (6) The framework is generalizable allowing control-oriented predictions beyond the training data. A simple interpolation-based control-oriented extension of CNM is proposed and tested. Despite its simplicity, CNMc accurately predicts the state dynamics at new operating conditions over the entire sample record.

CNM is found to have a distinct superiority over cluster-based Markov models, namely the much longer prediction horizon as evidenced by the autocorrelation function. The modeling and prediction capabilities are demonstrated on a number of examples exhibiting chaos, rare events, and high-dimensionality. In all cases, the dynamics are remarkably well represented with CNM; The temporal evolution of the main flow dynamics, the fluctuation level, the autocorrelation function, and the cluster population are all accurately reproduced.

CNM opens a novel automatable avenue for data-driven nonlinear dynamical modeling and real-time control. It holds the potential for a myriad of further research directions. Its probabilistic foundations are naturally extendable to include uncertainty quantification and propagation. One limiting requirement of CNM is the relatively large statistically-converged training data it requires compared to other known methods (e.g. ARMA and SINDy). This requirement could be relaxed through explicit coupling to first-principle equations. The control-oriented extension may be further refined and more broadly implemented on other applications.

Acknowledgments

We are grateful to Themistoklis Sapsis, Steve Brunton, Wolfgang Schröder and Marian Albers for the stimulating discussions and for providing some of the employed data. **Funding:** The research was funded by the Deutsche Forschungsgemeinschaft (DFG) in the framework of the research projects SE 2504/2-1. **Authors contributions:** B.R.N. conceptualized the algorithm. B.R.N., R.S. and D.F. performed the investigation, data analysis and interpretation. R.S. and D.F. wrote the manuscript and D.F. implemented the software. **Competing interests:** The authors declare no competing interests. **Data and materials availability:** A CNM Python package along with the data used for this study are available in the github repository at github.com/fernexda/cnm.

Appendix A Problem settings

Cluster-based network modeling is applied to numerous examples, ranging from analytical systems to real-life problems using experimental and simulation data. The main results are summarized in Fig. 4. The first two applications are the Lorenz [26] and Rössler [28] attractors, typical candidates for dynamical systems analysis. The following two implementations are one-dimensional systems: electrocardiogram measurements (ECG) [29], and the dissipative energy from a Kolmogorov flow [30]. The last CNM application is a high-dimensional large eddy simulation of an actuated turbulent boundary layer for skin friction reduction [31].

In this section, we detail the various systems including the numerical setup and the CNM modeling parameters. CNM is fully parametrized by the number of clusters K and the model order L . Their selection plays an important role in the model accuracy. The values used for the various systems are listed in Table 1. The procedure to select K and L is detailed in Appendix C. The last column in Table 1 lists the normalized time delays t_L/T_0 , where T_0 is the fundamental period computed from the dominant frequency identified from the autocorrelation function. For purely random signals with no deterministic component, such as the dissipative energy of the Kolmogorov flow, no characteristic period can be defined. As indicated by the table,

Table 1: **CNM settings for all applications.** The number of clusters K and the model order L are listed for the five systems. The last column t_L/T_0 designates the normalized time delay corresponding to the selected model order L . The fundamental period T_0 is computed from the dominant frequency of the system, when possible.

System	Number of clusters K	Model order L	t_L/T_0
Lorenz	50	22	1.7
Rössler	100	2	0.6
ECG	50	23	0.14
Kolmogorov flow	200	25	-
Boundary layer	50	3	0.25

the CNM parameters are strongly dependent on the nature of the systems dynamics. Physical interpretation of the chosen parameters is provided for each system in the following.

Lorenz system

The Lorenz system [26] is a typical candidate for dynamical system analysis. Despite its low dimension, it exhibits a chaotic behavior. The motion is characterized by periodic oscillations of growing amplitude in the 'ears' and a random switching between them. The Lorenz system is driven by a set of three coupled nonlinear ordinary differential equations (ODEs) given by

$$\begin{aligned}
 \frac{dx}{dt} &= \sigma(y - x) \\
 \frac{dy}{dt} &= x(\rho - z) - y \\
 \frac{dz}{dt} &= xy - bz.
 \end{aligned} \tag{9}$$

The selected parameters are $\sigma = 10$, $\rho = 28$, and $\beta = 8/3$ with initial conditions $(-3, 0, 31)$. The simulation is performed with a time step $\Delta t = 0.015$ for a total of 57 000 samples. The

numerical integration is performed with the explicit Runge-Kutta method of 5th order using the `scipy` library from the `python` programming language [33, 34].

The relatively high number of clusters ($K = 50$) ensures that each wing is resolved by two orbits of centroids (see the phase space clustering in Fig. 4), and allows to reproduce some of the increasing oscillation amplitude. K can be increased (decreased) to resolve more (less) orbits in each ear. Due to the dynamics complexity and especially the random ear flipping, the Lorenz system requires a large time delay t_L equivalent to 1.7 rotation. With lower L values, the trajectory that reaches the ears intersection becomes more likely to wrongly switch sides.

Rössler system

The Rössler is a three-dimensional system governed by non-linear ordinary differential equations [28] that read

$$\begin{aligned}\frac{dx}{dt} &= -y - z \\ \frac{dy}{dt} &= x + ay \\ \frac{dz}{dt} &= b + z(x - c).\end{aligned}\tag{10}$$

where the parameters are $a = 0.1$, $b = 0.1$, and $c = 14$. The initial conditions are set to $(1, 1, 1)$ and the simulation is performed with a time step $\Delta t = 0.01$ for a total of 50 000 samples. The Rössler data is also created with the `scipy` library using the explicit Runge-Kutta method of 5th order. Similar to the Lorenz system, the Rössler is widely used for dynamical system analysis. The system also yields chaotic behavior under specific parameters combinations. The motion is characterized by rotations of slowly growing amplitude in the x - y plane, and intermittent peaks in the z direction.

The Rössler system requires a large number of clusters to ensure a sufficient centroid coverage in the peak for an accurate reproduction of this intermittent and fast event. However, since the trajectory itself is relatively simple, a time-delay t_L of approximately half of the characteristic period is sufficient ($t_L/T_0 = 0.6$).

Electrocardiogram signal

An electrocardiogram (ECG) measures the heart activity over time. Electrodes are placed on the person's skin to deliver an univariate voltage of the cardiac muscle movements. The time series exhibit the typical pulse associated with the heart beat. The ECG signal used in this study is from the PhysioNet database [35]. The signal time range is 180 seconds and the sampling frequency is 250 Hz.

Similarly to the Rössler, the ECG requires a large number of clusters K in order to resolve the quasi-circular phase space trajectory corresponding to the fast heartbeat pulse. Again, due to the very regular and repetitive nature of the heart activity, a small time delay t_L is sufficient.

Kolmogorov flow

The Kolmogorov flow is a two-dimensional generic flow defined on a square domain $\mathbf{q} = (x, y)$ with $0 \leq x \leq L$ and $0 \leq y \leq L$, subject to a horizontal sinusoidal forcing \mathbf{f} , defined by

$$\mathbf{f}(x) = \sin(a y)\mathbf{e}_1, \quad (11)$$

where $\mathbf{e}_1 = (1, 0)^T$ is a unit vector in the x direction. The Kolmogorov flow is a test-bed for various fluid mechanics and turbulence studies [36]. The temporal evolution of the flow energy E , the dissipative energy D and input energy I are defined by

$$E(t) = \frac{1}{2L^2} \iint |\mathbf{u}(\mathbf{q}, t)|^2 d\mathbf{q} \quad (12)$$

$$D(t) = \nu \frac{1}{L^2} \iint |\boldsymbol{\omega}(\mathbf{q}, t)|^2 d\mathbf{q} \quad (13)$$

$$I(t) = \frac{1}{L^2} \iint |\mathbf{u}(\mathbf{q}, t) \cdot \mathbf{f}(\mathbf{q}, t)|^2 d\mathbf{q} \quad (14)$$

where ν is the fluid viscosity and $\boldsymbol{\omega}$ is the vorticity. The rate of change of the energy is equal to the input energy minus the dissipation energy, as $\dot{E} = I - D$. With increasing forcing wave number a , the dissipation energy yields intermittent and random bursts. This behavior makes the dissipation energy a good candidate for rare events modeling. The current data were created and generously shared by Farazmand et al. [37], with a wavenumber $a = 4$ and a Reynolds number $Re = 40$. The total time range is 100 000 dimensionless time units with a sampling frequency of 10.

The trajectory in the phase space spanned by D and its temporal derivative \dot{D} (Fig. 4) is particularly complex. The region with higher clusters density in the left region of the phase space corresponds to the random fluctuations, and the region with sparser centroids distribution describes the intermittent energy bursts. Due to its stochastic nature and the absence of deterministic patterns, the Kolmogorov flow dissipation energy has been particularly challenging to model. Remarkably, with sufficiently large K and L , CNM is capable of modeling D with high accuracy.

Actuated turbulent boundary layer

The reduction of viscous drag is crucial for many flow-related application such as airplanes and pipelines, as it is a major contributor to the total drag. Many passive [38, 39] and active [40, 41] actuation techniques have been investigated to reduce the skin-friction drag. In this study, skin-friction reduction on a turbulent boundary layer is achieved by means of a spanwise traveling surface wave [31, 42].

The waves are defined by their wavelength λ^+ , period T^+ and amplitude A^+ . The superscript $+$ denotes variables scaled with the friction velocity and the viscosity. Details about the computational setup can be found in Albers et al. [31]. The actuation parameters are $\lambda^+ = 1000$,

$T^+ = 120$, $A^+ = 60$. The total time range in $^+$ units is 846 and the sampling frequency is 0.5, resulting into 420 snapshots. The velocity field is given by $\mathbf{u}(\mathbf{q}, t^+)$, where $\mathbf{q} = (x^+, y^+, z^+)$ in the Cartesian coordinates with $x^+ \in [2309, 4619]$, $y^+ \in [0, 692]$ and $z^+ \in [0, 1000]$.

Clustering of large high-dimensional datasets is costly. The required distance computation between two snapshots \mathbf{u}^m and \mathbf{u}^n

$$d(\mathbf{u}^m, \mathbf{u}^n) = \|\mathbf{u}^m - \mathbf{u}^n\|_{\Omega} \quad (15)$$

is computationally very expensive. Here, the norm is defined as

$$\|\mathbf{u}\|_{\Omega} = \sqrt{(\mathbf{u}, \mathbf{u})_{\Omega}} \quad (16)$$

and the inner product in the Hilbert space $\mathcal{L}(\Omega)$ of square-integrable vector fields in the domain Ω is given by

$$(\mathbf{u}, \mathbf{v})_{\Omega} = \int_{\Omega} \mathbf{u}(\mathbf{q})\mathbf{v}(\mathbf{q}) \, d\mathbf{q}. \quad (17)$$

For high-dimensional data such as the boundary layer velocity field, data compression with loss-less proper orthogonal decomposition (POD) can reduce the computational cost of clustering. Here, a snapshot \mathbf{u}^m is exactly expressed by the POD expansions as

$$\mathbf{u}(\mathbf{q}, t) = \mathbf{u}_0(\mathbf{q}) + \sum_{i=0}^{M-1} a_i(t)\Phi_i(\mathbf{q}), \quad (18)$$

where \mathbf{u}_0 is the mean flow, Φ_i denotes the POD modes, and $a_i(t)$ the corresponding mode coefficients. As shown by Kaiser et al. [19], the distance computation (15) can be alternatively performed with the mode coefficients instead of the snapshots, as

$$d(\mathbf{u}^m, \mathbf{u}^n) = \|\mathbf{u}^m - \mathbf{u}^n\|_{\Omega} \quad (19)$$

$$= \|\mathbf{a}^m - \mathbf{a}^n\|. \quad (20)$$

Hence, $\mathbf{a}^m = [a_1^m, \dots, a_{M-1}^m]$ becomes the POD representation of snapshot m at time $t^m = m\Delta t$. Eq. (20) is computationally much lighter than (19). Despite the additional autocorrelation matrix computation for the POD process, the data compression procedure remains very beneficial for large numerical grids. According to [20], the computational savings amount to

$$\frac{M+1}{2J \times I \times K}, \quad (21)$$

where M is the number of snapshots, K the number of clusters, I the number of k -means inner iterations, and J is the number of random centroids initializations. For typical values ($K \sim 10$, $I \sim 10K$, and $J \sim 100$), the saving are one or two orders magnitude. Furthermore, POD is computed only once for each dataset and will benefit all future clusterings performed on that dataset.

The actuated turbulent boundary layer at the used actuation settings exhibits synchronization with the actuation wave. The dynamics show quasi limit-cycle behavior with superimposed wandering. Therefore, a low number of centroids are sufficient to capture the dynamics. If desired, the limit-cycle meandering associated with higher frequency turbulence can be resolved with a larger set of centroids. The selected value of $K = 50$ is a compromise between a sufficient resolution of the turbulence scales (64% of the data fluctuation is resolved) and a reasonable model complexity. The dynamics are well captured with a low model order L , equivalent to a time-delay of a quarter of the actuation period.

Appendix B Cluster-based network modeling methodology

Robust probability-based data-driven dynamical modeling for complex nonlinear systems has the potential to revolutionize our ability to predict and control these systems. Cluster-based network models (CNM) reproduces the dynamics on a directed network [15], where the nodes are the coarse-grained states of the system. The transition properties between the nodes are based on high-order direct transition probabilities identified from the data. The model methodology is applied to a variety of dynamical systems, from canonical problems such as the Lorenz attractor to rare events to high degrees of freedom systems such as a boundary layer flow simulation. The general methodology is illustrated in Fig. 1 with the Lorenz system and is detailed in the following.

The first step is the data collection, where a set of M states \mathbf{x}^m , $m = 1, \dots, M$, also called observations or snapshots, are collected from a dynamical system. They are equally spaced in time by Δt , so that $\mathbf{x}^m = \mathbf{x}(m\Delta t)$. There is no restriction regarding the type of system nor the state dimension.

The second step is the identification of the network nodes using an unsupervised clustering algorithm that groups the snapshots into K clusters \mathcal{C}_k , $k = 1, \dots, K$. In this study, we employ the k -means++ algorithm [43, 44, 23] for its simplicity and ability to compute physically meaningful and interpretable centroids. The algorithm performs an iterative search for an optimal centroid distribution that increases the inner-cluster similarity, by executing the following steps:

Step 1: The initial centroid distribution \mathbf{c}_k is randomly generated.

Step 2: Each snapshot is affiliated to its closest centroid, following the cluster affiliation function k defined as

$$k(\mathbf{x}^m) = \arg \min_i \|\mathbf{x}^m - \mathbf{c}_i\|, \quad (22)$$

where $\|\mathbf{x}\| = \sqrt{\mathbf{x} \cdot \mathbf{x}}$. The function k maps, for each state \mathbf{x}^m , the index of the closest centroid.

Step 3: The inner-cluster variance J of this centroid distribution is computed as

$$J(\mathbf{c}_1, \dots, \mathbf{c}_K) = \sum_{k=1}^K \sum_{\mathbf{x}^m \in \mathcal{C}_k} \|\mathbf{x}^m - \mathbf{c}_k\|^2. \quad (23)$$

Step 4: The centroid positions are updated by averaging the state snapshots within the corresponding cluster

$$\mathbf{c}_k = \frac{1}{n_k} \sum_{\mathbf{x}^m \in \mathcal{C}_k} \mathbf{x}^m, \quad (24)$$

where n_k is the number of snapshots in cluster \mathcal{C}_k .

Steps 2 to 4 are repeated until the inner-cluster variance J is minimized below a specified tolerance. Let the vector $\mathcal{K} = [\mathcal{K}_1, \dots, \mathcal{K}_I]$, $\mathcal{K}_i \in [1, K]$ contain the indexes of all consecutively visited clusters over the entire time sequence, such that \mathcal{K}_i is the index of the i th visited cluster. The first and last clusters are $\mathcal{C}_{\mathcal{K}_1}$ and $\mathcal{C}_{\mathcal{K}_I}$, respectively. The size I of \mathcal{K} is equal to the number of transitions between K centroids over the entire ensemble plus one. The transition time between the sequential clusters is not constant and depends on the state velocity in the phase space. The vector \mathcal{K} constitutes the starting point to identify the transition properties between the centroids.

Following the identification of the centroids as the network nodes, the third step of the CNM algorithm characterizes the motion along the nodes. The dynamics are constructed as linear transitions between centroids based on the transition probabilities and the transition times. After a centroid is reached, the next destination is identified using the direct transition probability tensor \mathbf{Q} . The tensor \mathbf{Q} ignores inner-cluster residence probability and only considers inter-cluster transitions. One novelty of this CNM implementation is to model the direct transition probabilities \mathbf{Q} using an L -order Markov model, which is defined as a conditional probability $\Pr(\mathcal{K}_i | \mathcal{K}_{i-1}, \dots, \mathcal{K}_{i-L})$. In this context, high-order Markov models are equivalent to time-delay embedding, which are well known in dynamical systems [25]. The benefit of time-delay coordinates is elaborated in Appendix E. For a second-order model, $\mathbf{Q} \in \mathcal{R}^{K \times K \times K}$ is a third-order tensor and the probability to move to \mathcal{C}_l , having previously visited \mathcal{C}_k and \mathcal{C}_j , is inferred from the data and given by

$$Q_{l,k,j} = \Pr(\mathcal{K}_i = l | \mathcal{K}_{i-1} = k, \mathcal{K}_{i-2} = j) = \frac{n_{l,k,j}}{n_{k,j}}. \quad (25)$$

$n_{l,k,j}$ designates the number of transitions to \mathcal{C}_l , having previously visited \mathcal{C}_j and \mathcal{C}_k , and $n_{k,j}$ is the number of transitions departing from \mathcal{C}_k coming from \mathcal{C}_j , regardless of the destination. Note that inner cluster iterations are not possible, by the very definition of a direct transition, such that $Q_{j,j} = \Pr(\mathcal{K}_i = j | \mathcal{K}_{i-1} = j) = 0$.

The transition time designates the time required to travel from one centroid to the next. In this CNM implementation, the transition time is defined as half of the sum of the residence times in two sequential clusters, as illustrated in Fig. 2 for a first-order model. Let t^n and t^{n+1}

be the time of the first and last snapshots to enter and, respectively, leave \mathcal{C}_k at the n th iteration. The iterations designate the sequential jumps between the centroids. The residence time τ^n in \mathcal{C}_k is

$$\tau^n := t^{n+1} - t^n. \quad (26)$$

Following this definition, the individual transition time $\tau_{k,j}^n$ from centroid \mathbf{c}_j to centroid \mathbf{c}_k is given by

$$\tau_{k,j}^n = \frac{t^{n+1} - t^{n-1}}{2} = \frac{\tau^{n-1} + \tau^n}{2}. \quad (27)$$

The transition time $T_{k,j}$ is the average of all transition times $\tau_{k,j}^n$ between centroids \mathbf{c}_j and \mathbf{c}_k as

$$T_{k,j} = \frac{1}{n_{k,j}} \sum_{n=1}^{n_{k,j}} \tau_{k,j}^n. \quad (28)$$

Consistent with the direct transition matrix \mathbf{Q} for an L -order chain, the transition time \mathbf{T} also depends on the $L - 1$ previously-visited centroids.

For large time delays (hence large L), the process could yield to two storage-intensive $L + 1$ -dimensional tensors \mathbf{Q} and \mathbf{T} with K^{L+1} elements. For instance, clustering with $K = 20$ clusters and an order $L = 10$, the tensors would contain 20^{11} elements, which exceeds the storage capacities of most computers. The expensive tensor creation and storage is circumvented by a lookup table (LUT), where only non-zero entries that correspond to actual transitions are retained. Thus, the tensors are replaced by a simple array indexing operation. The look-up tables are typically orders-of-magnitude smaller than the full tensors. As illustration, let's consider the example in Fig. 1 but with fictional transition properties. Here, all centroids have only one possible destination, except \mathbf{c}_2 , where the state can transit to either \mathbf{c}_3 or \mathbf{c}_5 with an assumed equal probability for simplicity ($Q_{3,2,1} = Q_{5,2,1} = 0.5$). The 2nd-order LUT for this example is illustrated in Table 2. The transition times are randomly chosen for this fictional example. If the state is in \mathbf{c}_2 ($k = 2$) having visited \mathbf{c}_1 before ($j = 1$), the next destination is probabilistically chosen between $Q_{3,2,1}$ and $Q_{5,2,1}$ (lines 5 and 7), yielding a transition to either centroid 3 or centroid 5. If the selected destination is \mathbf{c}_5 , the corresponding time to this transition is read from $T_{5,2,1}$ (entry # 7).

The fourth and final step of the CNM procedure is state propagation. We assume a linear motion between the centroids. The instantaneous state between two centroids \mathbf{c}_j and \mathbf{c}_k is defined as

$$\mathbf{x}(t) = \alpha_{kj}(t)\mathbf{c}_k + [1 - \alpha_{kj}(t)]\mathbf{c}_j, \text{ with } \alpha_{kj} = \frac{t_j - t}{T_{k,j}}, \quad (29)$$

where t_j is the time when the centroid \mathbf{c}_j is left and $T_{k,j}$ is the transition time from \mathbf{c}_j to \mathbf{c}_k . The motion between the centroids may be interpolated with splines for smoother trajectories. As CNM is purely data-driven, the model quality is directly related to that of the training data. More specifically, the sampling frequency and total time range must be selected, such that all relevant dynamics are captured and are statistically converged.

Table 2: **Lookup table (LUT) of the transition properties.** The storage-intensive $L + 1$ -dimensional tensors \mathbf{Q} and \mathbf{T} with K^{L+1} elements are replaced by a lookup table, where only non-zero entries that correspond to actual transitions are retained. The storage requirements are orders of magnitude smaller than that of the full tensors.

#	l	k	j	$Q_{l,k,j}$	$T_{l,k,j}$
1	1	4	3	1	2
2	1	6	5	1	1
3	2	1	4	1	0.5
4	2	1	6	1	0.25
5	3	2	1	0.5	2
6	4	3	2	1	4
7	5	2	1	0.5	1
8	6	5	2	1	2

Appendix C Validation

This section presents two metrics used to evaluate the model performance, namely the autocorrelation function and the cluster probability vector. We note the occasional need for additional or different metrics to validate models of certain systems, such as the probability distribution function of a system with rare events.

Autocorrelation function

The direct comparison of time series of complex systems is often pointless, as the trajectories might rapidly diverge even when the dynamical features are preserved. This is especially true for chaotic systems, where a slight change in initial conditions leads to completely different trajectories. Following Protas et al. [27], the cluster network model is validated based on the computed and predicted autocorrelation function of the state vector, defined as

$$R(\tau) = \frac{1}{T - \tau} \int_0^{T-\tau} (\mathbf{x}(t), \mathbf{x}(t + \tau)) dt, \tau \in [0, T]. \quad (30)$$

where (\cdot, \cdot) designates the inner product, defined as

$$(\mathbf{x}, \mathbf{y}) = \mathbf{x} \cdot \mathbf{y}^T. \quad (31)$$

This function avoids the problem of comparing two trajectories with finite dynamic prediction horizons due to phase mismatch. The autocorrelation function also yields the fluctuation energy at vanishing delay $R(\tau = 0)$ and can be used to infer the spectral behavior.

In case of the cluster-based Markov model (CMM) (c.f. Appendix E), the time integration quickly leads to the average state and is not indicative for the range of possible initial conditions.

Hence, K trajectories are considered starting sequentially in each of the K clusters, such that $\mathbf{p}^k(t = 0) = [\delta_{1k}, \dots, \delta_{Kk}]^T$, where δ is the Dirac delta function. The autocorrelations are weighted with the cluster probability p_k^∞ as,

$$\hat{R}(\tau) = \sum_{k=1}^K p_k^\infty \frac{1}{T - \tau} \int_0^{T-\tau} (\hat{\mathbf{x}}^k(t), \hat{\mathbf{x}}^k(t + \tau)) dt, \tau \in [0, T], \quad (32)$$

where $\hat{\mathbf{x}}^k$ is the CMM-modeled trajectory initialized in centroid k .

Cluster probability distribution

The cluster probability distribution $\mathbf{p} = [p_1, \dots, p_K]$, provides the probability to be in a specific cluster. It indicates whether the model trajectories populate the phase space similarly to the reference data. The cluster probability distribution of the reference data is computed as

$$p_k = \frac{n_k}{M}, \quad (33)$$

where n_k is the number of snapshots affiliated to cluster \mathcal{C}_k and M is the total number of snapshots. In CMM, the state is iteratively propagated with time steps Δt , so that $t^l = l\Delta t$. The asymptotic cluster probability distribution for CMM \mathbf{p}^∞ is determined for $l \rightarrow \infty$ by

$$\mathbf{p}^\infty = \lim_{l \rightarrow \infty} \mathbf{P}^l \mathbf{p}^0, \quad (34)$$

where \mathbf{p}^0 is the initial condition and \mathbf{P} is the transition matrix (c.f. Appendix E). For CNM, the asymptotic probability distribution p_k^∞ is obtained for a long-enough time horizon T_0 as the sum of the residence times τ^i in \mathcal{C}_k divided by the total simulation time,

$$p_k^\infty = \frac{\sum \tau^i}{T_0}. \quad (35)$$

The cluster probability distributions for the data, CMM, and CNM with varying order are presented in Fig. 10 and discussed in Appendix E.

Appendix D Parameters selection

CNM is parametrized by the number of clusters K and the model order L . Both parameters are problem-dependent and can be optimized to achieve the highest prediction accuracy. This section details the current parameters selection process and provides guidelines and recommendations for other datasets.

The number of clusters K determines the resolution level. A small number of clusters will mostly capture the dominant behavior at the macro level, which is suitable for simple dynamics such as a limit cycle. Few centroids also enable easier interpretation of the results and

physical insights. Higher K allows to accurately model more complex systems, possibly at the micro scale level, and to uncover a broader range of dynamics including transitional events and higher frequency components. Excessively large K values could be however detrimental, as adjacent trajectories get clustered separately despite describing nearly the same motion. Furthermore, the trajectory of an over-clustered system might introduce an artificial low-amplitude and high frequency noise component resulting from sequential small jumps between misaligned centroids.

The model order L is synonymous with time-delay embeddings in units of past centroids. Increasing L allows modeling of more realistic trajectories, especially when the dynamics have centroids located at the intersections of multiple trajectories, as illustrated in Fig. 8. In this example, trajectory 1 propagates sequentially through centroids $2 \rightarrow 1 \rightarrow 3$ and trajectory 2 through centroids $4 \rightarrow 1 \rightarrow 5$. With a first-order model, the state at c_1 can possibly transit to c_3 or to c_5 , regardless of the previous path. Such a low-order model is thus associated with an increased risk of selecting the wrong trajectory. With a second-order model, however, the previous centroid is taken into account in the conditional probability and the transition from c_1 remains on the correct trajectory, ensuring a more accurate motion. Complex dynamics with multiple intersected trajectories require larger order L . For better interpretability, L can be converted into the approximate corresponding time delay t_L , defined as

$$t_L = L\bar{T}, \quad (36)$$

where \bar{T} is the overall average transition time.

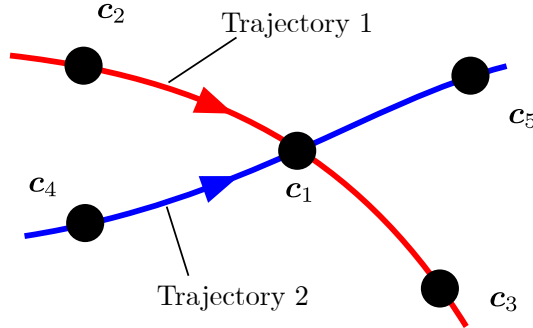


Fig. 8. Improved accuracy with higher model order L . In this example, trajectory 1 and 2 intersect at c_1 . With $L = 1$, the state can possibly leave the trajectory it is following, *e.g.* trajectory 1, and wrongly transit to trajectory 2 after leaving centroids c_1 . A 2nd-order model ensure that the state remains on the correct trajectory.

The values of K and T are problem-dependent. In this work, K and L are selected from a parametric study that minimizes the root mean square error (RMSE) of the autocorrelation function $R(\tau)$ of the reference data and that of the model (see Appendix C for details about

$R(\tau)$), defined as

$$\text{RMSE} = \sqrt{\frac{1}{N_R} \sum_{n=1}^{N_R} (R_n - \hat{R}_n)^2}, \quad (37)$$

where \hat{R} is the modelled autocorrelation and N_R is the maximum lag number. The RMSE distribution for the Lorenz system for varying K and L is presented in Fig. 9A. The results are shown for a range of $K \in [10, 100]$, and normalized time delay $t_L/T_0 \in [0.5, 1.8]$, where T_0 is the fundamental period of the system. The black dots denote the computed configurations. The RMSE does not change linearly with the number of cluster and the model order. The error distribution exhibits regions of high and low error. A low K and low L configuration produces poor dynamics (Fig. 9B), which is expected for a complex system like the Lorenz. As K and L increase, the error generally decreases, despite local maxima (Fig. 9C). The configuration indicated with the red dot (Fig. 9D) is selected for its high accuracy, which is comparable to other more complex models (e.g., Fig. 9E). This winning configuration consists of $K = 50$ clusters and an order $L = 22$, that corresponds to $t_L/T_0 = 1.7$.

Appendix E Comparison between CNM and CMM

The CNM implementation presented in this study builds on two prior cluster-based modeling methods. The first, labelled cluster-based Markov model (CMM), propagates the state using a Markov chain with a constant time step [19]. The second is the initial CNM implementation, which introduced realistic transition times between clusters that yielded a more accurate dynamics [45, 20]. The present work extends CNM to high-order chains for both the transition probability and the transition time. The resulting drastic improvements over the two preceding methods are demonstrated in this section using the Lorenz system as example.

The starting point for CMM and both CNM variants is the clustering of the snapshots into K clusters \mathcal{C}_k (for details on the clustering algorithm, see Appendix B). Clustering reduces and coarse-grains the original potentially high-dimensional data into a set of centroids \mathbf{c}_k . Both methodologies are described in the main manuscript and are briefly summarized in the following. In CMM, the state variable is $\mathbf{p} = [p_1, \dots, p_K]$, where p_k is the probability of being in cluster \mathcal{C}_k . The transition from centroid \mathbf{c}_j to \mathbf{c}_i is guided by the probability transition matrix $\mathbf{P} = (P_{ij}) \in \mathcal{R}^{K \times K}$. The propagation of \mathbf{p} in time is performed iteratively in steps of Δt and is given at time $t^l = l\Delta t$ by

$$\mathbf{p}^{l+1} = \mathbf{P}\mathbf{p}^l. \quad (38)$$

The state \mathbf{x} at time t^l is given by

$$\mathbf{x}(t^l) = \sum_{k=1}^K p_k(t^l) \mathbf{c}_k. \quad (39)$$

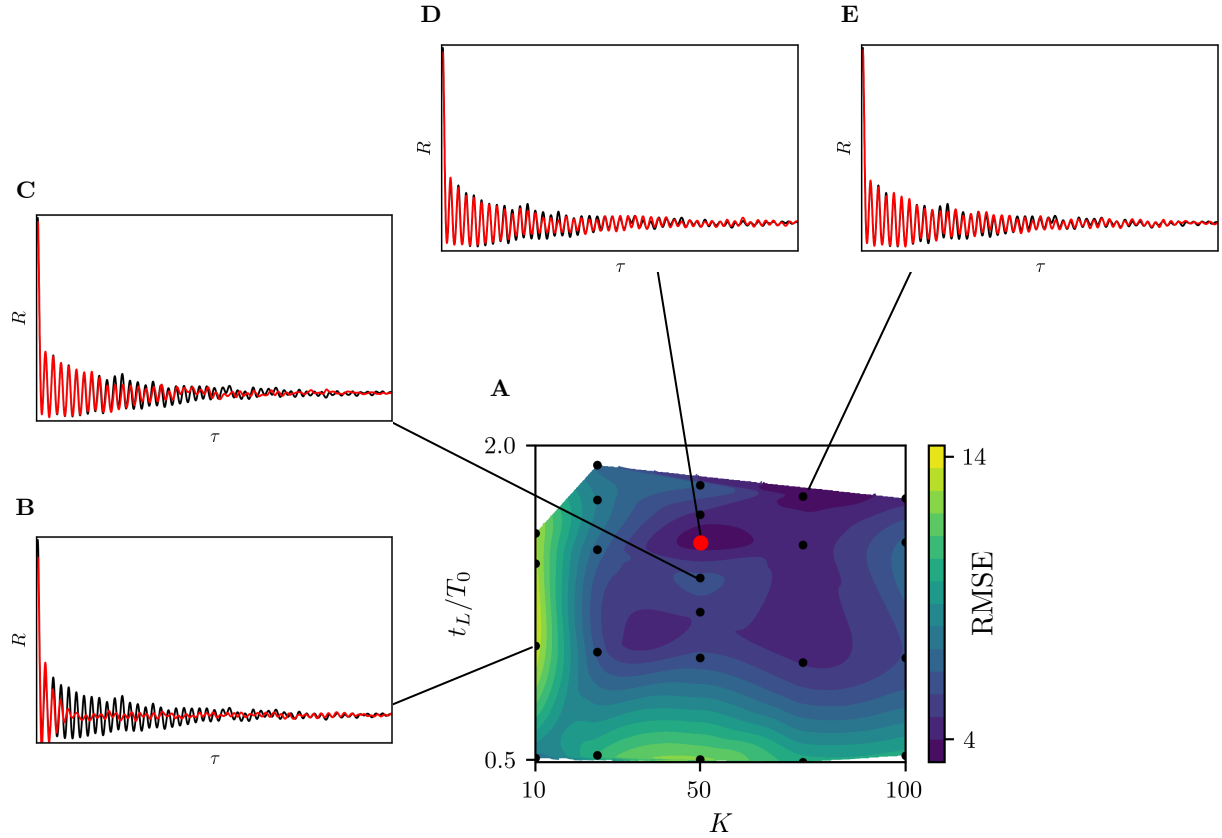


Fig. 9. Selection of the number of centroids K and model order L . (A) Root-mean square error distribution of the autocorrelation function $R(\tau)$ of the reference data and that of the model for the Lorenz system. The results are shown for a range of $K \in [10, 100]$ and normalized time delays $t_L/T_0 \in [0.5, 1.8]$, where T_0 is the fundamental period of the system. The winning configuration is indicated with a red dot. (B) to (E) Autocorrelation function of the data (black) and CNM (red) for varying K and L . A small number of centroids $K = 10$ produces poor dynamics (B). The distribution presents local minima and maxima (C). The agreement between the reference and modeled $R(\tau)$ increases for larger K and L values ((D) and (E)).

Despite its ability to provide insights into the guiding mechanisms of various physical systems [46, 47], CMM fails at modeling the dynamics. The state vector of cluster probabilities ultimately and unavoidably diffuses to a fixed point representing the post-transient attractor.

The initial CNM version addresses this issue by introducing realistic transition times. At each iteration, the state shifts to a subsequent cluster in a data-inferred time. The direct transition probabilities Q and transition times T are $K \times K$ zero-diagonal matrices, which result from the state switching centroids at each iteration. The data-inferred transition times drastically increase accuracy compared to CMM, especially for periodic dynamics. This algorithm is, however, not well-suited for complex phase-space trajectories and long time-horizon predictions. The present CNM variant extends the algorithm to high-order Markov models, where both past and current states are jointly considered to determine the next destination cluster and the corresponding transition time. The optimal order is problem-dependent and can be optimized, as detailed in Appendix D. With this latest upgrade, CNM is now capable of modeling any complex nonlinear dynamical system.

The three methods are benchmarked on the Lorenz system, that is described in Appendix A. Clustering is performed with $K = 50$ clusters and the model order is set to $L = 22$. The cluster probability distribution, which indicates whether the model trajectories populate the phase-space similarly to the data, is depicted for the three methods in Fig. 10A. For clarity of presentation and interpretation, the results are shown for only 10 centroids instead of 50. The coarsening is performed by affiliating the CNM-generated snapshots to the closest of the 10 centroids. The converged probability distribution for CMM matches exactly that of the data, as already reported in the literature [19, 48], whereas those for both CNM variants yield a very good agreement.

The time series of the reference data and of the three models are shown in Fig. 10B to 10E. The reference time series (10B) depict the growing amplitude oscillations in both ears as well as the random ear switching. The CMM temporal evolution in 10C quickly asymptotes toward a fix value after a few oscillations, thus demonstrating the model inability to resolve any meaningful dynamics. Conversely, both CNM models appear to properly duplicate the reference time series (Fig. 10D and Fig. 10E).

The benefits of the high-order CNM become apparent when comparing the autocorrelation function distributions in Fig. 11. As expected, the autocorrelation function from CMM rapidly drops to zero (Fig. 11A). The first-order CNM roughly reproduces the first few iterations, but both amplitude and phase quickly diverge from those of the data (Fig. 11B). In contrast, the high-order CNM, accurately duplicates the oscillations amplitude and phase over the entire range and evidentiates the correct modeling of the dynamics (Fig. 11C).

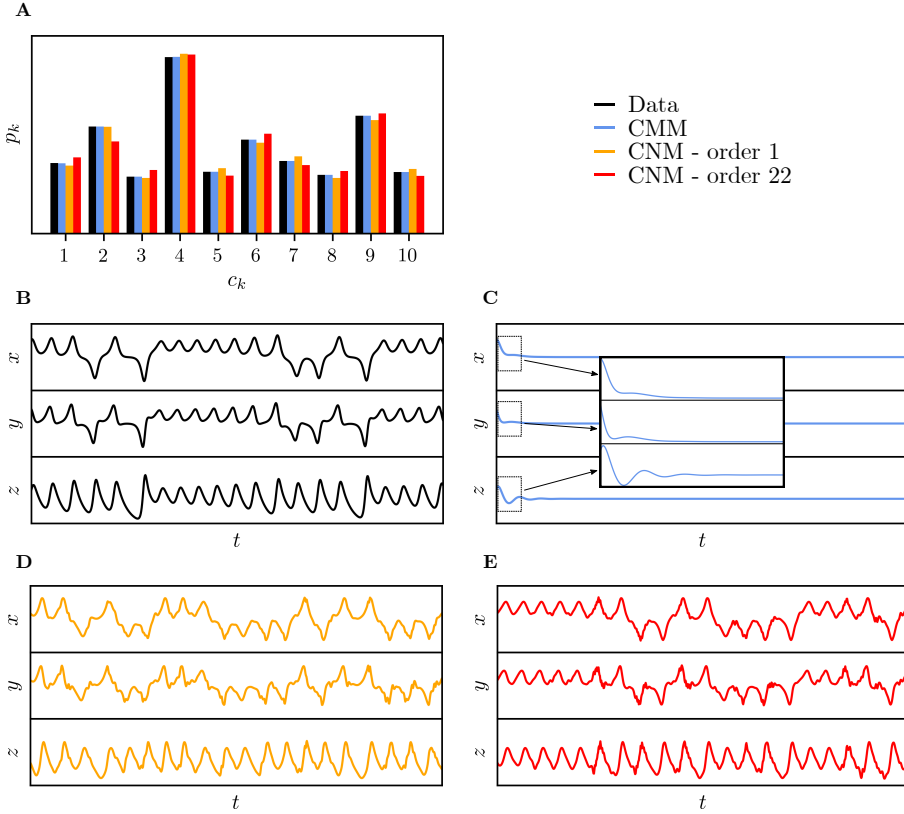


Fig. 10. Comparison of the cluster probability distributions and time series. (A) Cluster probability distribution of the data, CMM, 1st-, and 22nd-order CNM, respectively. The distributions are shown for 10 centroids for clarity. CMM reproduces exactly the probabilities of the reference data, whereas the CNM cluster probability distributions agree very well with the data. (B)-(E) Time series of the data, CMM, 1st-, and 22nd-order CNM, respectively. (C) The CMM model fails at predicting any dynamics. (D) and (E) Both CNM variants capture the oscillations and ear switching of the reference data.

Appendix F Control-oriented cluster-based network modeling

To disambiguate the effect of internal dynamics from actuation or external input, we generalize CNM to include control \mathbf{b} . This enables predictions beyond the training data for new control parameters $\hat{\mathbf{b}}$. The main steps of CNMc are illustrated in Fig. 12 and the algorithm is detailed in Algorithm 1.

Before we detail the algorithm, we introduce some of the relevant parameters and definitions. Let I be the number of test cases with I different control terms, where the superscript (i)

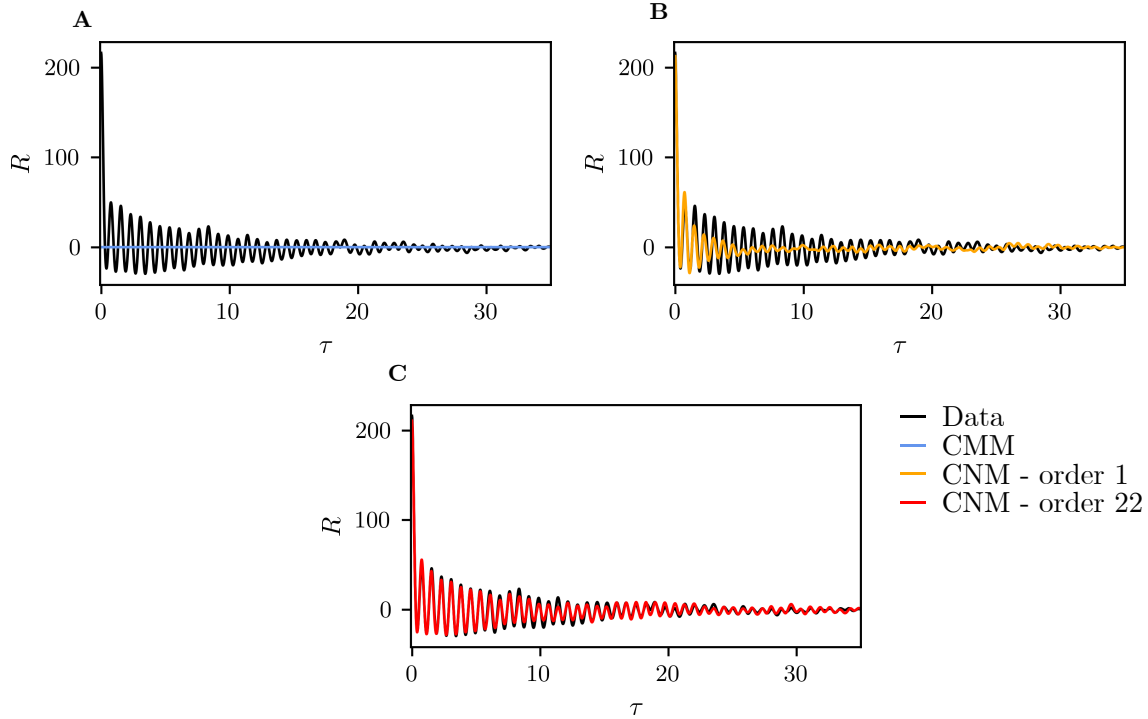


Fig. 11. Comparison of the autocorrelation function. Autocorrelation function of (A) the data, (B) CMM, (C) 1st-, and (D) 22nd-order CNM, respectively. The superiority of the high-order CNM over the two other methods is clearly visible. (A) CMM yields a flat autocorrelation function, demonstrating that no dynamics are resolved. (B) After a few oscillations, the first-order CNM prediction rapidly deteriorates. (C) The agreement of the 22nd-order model with the data is excellent over the entire time range and confirms the model long time-horizon prediction capabilities.

designate the i^{th} test case, $i = 1, \dots, I$. We denote the control term for the new to-be-predicted test case as $\hat{\mathbf{b}}$. The distance between two control terms \mathbf{b}^i and \mathbf{b}^j is defined by

$$d(\mathbf{b}^i, \mathbf{b}^j) = \|\mathbf{b}^i - \mathbf{b}^j\|, \quad (40)$$

where $\|\cdot\|$ designates the Euclidean norm. Similarly to all machine-learning methods, CNMc is inherently limited in its ability to extrapolate beyond the data range. Specifically, the control parameter $\hat{\mathbf{b}}$ must lie within the range of available control space. Since the method relies on interpolation, two neighboring test cases must be identified. Using the Euclidean distance (40), the two closest operating conditions with the shortest distance to $\hat{\mathbf{b}}$ are determined. Henceforth, the superscript (i) designates specifically these two neighboring operating conditions, such that $i = 1, 2$. The snapshots of these two operating conditions are separately grouped into K clusters $\mathcal{C}_k^{(i)}$, $k = 1, \dots, K$. Following CNM for individual operating conditions (see Appendix B), the

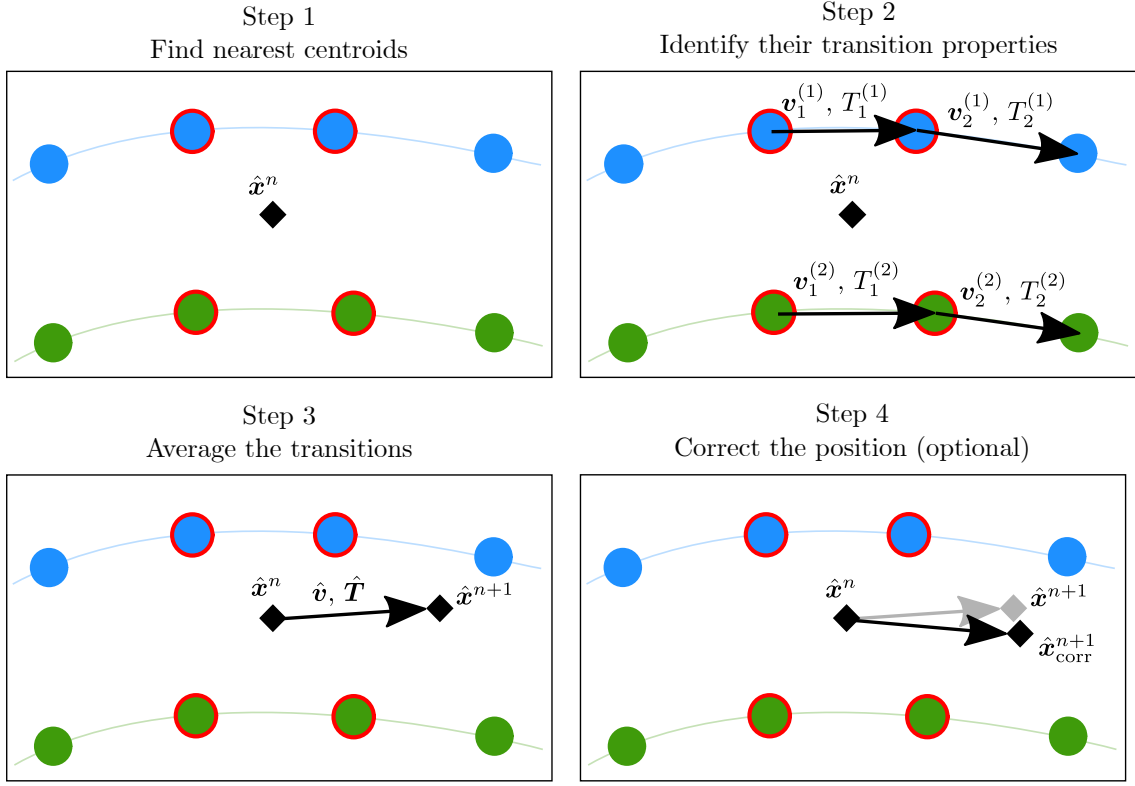


Fig. 12. Main steps of CNMc. The centroids of two neighboring test cases are identified. The state \hat{x} is propagated following 4 steps. Step 1: The nearest centroids $\mathbf{c}_{n_k}^{(i),n}$ to the current state \hat{x}^n are determined (red outer circles). Step 2: The transition vector $\mathbf{v}_{n_k}^{(i)}$ and transition time $T_{n_k}^{(i)}$ of each nearest centroid are identified. Step 3: The transition to the new position \hat{x}^{n+1} is set by $\hat{\mathbf{v}}$ and \hat{T} , which are the average of the nearest neighbors transition vectors and transition times, respectively. Step 4: For some systems, an additional position correction is needed to avoid a drift of the trajectory toward one of the two attractors. These steps are repeated until the total simulation time is reached.

transition probabilities $Q^{(i)}$ and transition times $T^{(i)}$, of each operating condition are separately computed. For a realistic initialisation of the new to-be-predicted system, the initial state \hat{x}_0 is computed as the average of a centroid from test case ($i = 1$) and its nearest neighbor from test case ($i = 2$).

Now that the two neighboring test cases are identified, the state of the new test case $\hat{\mathbf{b}}$ can be propagated. The motion propagation is performed iteratively, following the four steps illustrated in Fig. 12 and detailed in the following.

Step 1: For each neighboring operating condition (i), the N_k closest centroids to the state \hat{x}^n at iteration n are identified $\mathbf{c}_{n_k}^{(i),n}$, $n_k = 1, \dots, N_k$. The search is performed using a

k -d tree, that organizes the data in a tree-like structure to rapidly find nearest neighbors [49]. For low-dimensional data, the k -d tree distance metric is typically the Euclidean distance. For the high-dimensional boundary layer data, where the flow is driven by large scale actuation, an alternative norm that reduces high-frequency low-energy small scale contribution is recommended. One possible norm is the L_{10} norm, defined as $\|\mathbf{x}\|_{10} = (\sum_{i=1}^n |x_i|^{10})^{1/10}$, which favors the mode coefficients with large magnitude.

Step 2: The transition properties of the N_k nearest centroids are determined. The appropriate $L - 1$ past centroids of each neighboring centroid $\mathbf{c}_{n_k}^{(i),n}$ are identified by choosing from all possible trajectories leading to $\mathbf{c}_{n_k}^{(i),n}$ the most similar to the CNMc trajectory, as illustrated in Fig. 13 for a third-order model. In this example, the past centroids of $\mathbf{c}_{n_k}^{(i),n}$ along trajectory 2 are selected, since trajectory 2 is most aligned with $\hat{\mathbf{x}}$ up to this point. The next centroid $\mathbf{c}_{n_k}^{(i),n+1}$ and the transition time are identified from the corresponding \mathbf{Q} and \mathbf{T} . The motion direction is based on transition vectors $\mathbf{v}_{n_k}^{(i)}$ that span the transition from $\mathbf{c}_{n_k}^{(i),n}$ to $\mathbf{c}_{n_k}^{(i),n+1}$ as

$$\mathbf{v}_{n_k}^{(i)} = \mathbf{c}_{n_k}^{(i),n+1} - \mathbf{c}_{n_k}^{(i),n}. \quad (41)$$

For the first $L - 1$ iterations, the CNMc trajectory is not long enough to identify the $L - 1$ past centroids of the neighbors. In that case, the first $L - 1$ transition properties are identified from a first-order CNM model.

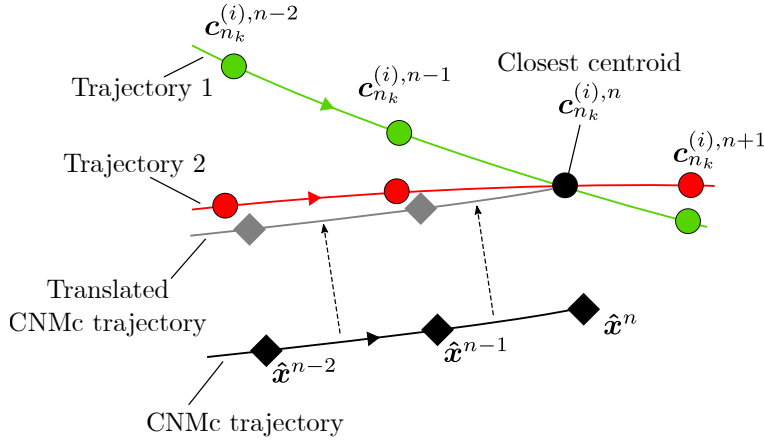


Fig. 13. Determination of the appropriate past trajectory. Example of a neighboring centroid $\mathbf{c}_{n_k}^{(i),n}$ to the predicted state $\hat{\mathbf{x}}$ with two possible past trajectories. The goal is to determine which of trajectories 1 or 2 is the most similar to the CNMc trajectory. First, the CNMc trajectory is translated so that $\hat{\mathbf{x}}^n$ coincides with $\mathbf{c}_{n_k}^{(i),n}$. Then, the past predicted states $\hat{\mathbf{x}}^{n-l}$ are sequentially compared to the previous centroids $\mathbf{c}_{n_k}^{(i),n-l}$ of trajectories 1 and 2, $l = 1, \dots, L - 1$. The trajectory with the smallest difference is selected as past for $\mathbf{c}_{n_k}^{(i),n}$. In this example, trajectory 2 is selected, since it is most aligned with the CNMc trajectory.

Step 3: The transition from $\hat{\mathbf{x}}^n$ to $\hat{\mathbf{x}}^{n+1}$ is fully characterized by the transition vector $\hat{\mathbf{v}}$ and the transition time \hat{T} , computed by averaging those of the $2N_k$ nearest centroids $\mathbf{c}_{n_k}^{(i),n}$. A weighted average can be employed to account for the distance from $\hat{\mathbf{b}}$ to $\mathbf{b}^{(1)}$ and $\mathbf{b}^{(2)}$. In the case where $\hat{\mathbf{b}}$ is equally distant to $\mathbf{b}^{(1)}$ and $\mathbf{b}^{(2)}$, \hat{T} and $\hat{\mathbf{v}}$ are computed as

$$\hat{T} = \frac{1}{2N_k} \sum_{i=1}^2 \sum_{n_k=1}^{N_k} T_{n_k}^{(i)}, \quad (42)$$

$$\hat{\mathbf{v}} = \frac{1}{2N_k} \sum_{i=1}^2 \sum_{n_k=1}^{N_k} \mathbf{v}_{n_k}^{(i)}. \quad (43)$$

The new position is $\hat{\mathbf{x}}^{n+1} = \hat{\mathbf{x}}^n + \hat{\mathbf{v}}$ and is reached in a corresponding time of $t^{n+1} = t^n + \hat{T}$.

Step 4: The optional final step is the position correction. Observations have shown that the predicted dynamics sometimes tend to slide toward one of the two neighboring operating conditions. To circumvent this issue, the position correction forces the state to have a constant relative distance between the two test cases (1) and (2). The distance $d^{(i)}$ between the predicted state $\hat{\mathbf{x}}$ and a neighboring test case (i) is defined as the distance between $\hat{\mathbf{x}}$ and the closest snapshot in this test case $\mathbf{x}^{(i)}$ as

$$d^{(i)} = d(\hat{\mathbf{x}}, \mathbf{x}^{(i)}) = \|\hat{\mathbf{x}} - \mathbf{x}^{(i)}\|. \quad (44)$$

The correction is formulated to ensure that the ratio r of the distances between the corrected position $\hat{\mathbf{x}}_{\text{corr}}^{n+1}$ and the two neighboring test cases is the same as that of the distances between $\hat{\mathbf{b}}$ and the two neighboring control inputs

$$r = \frac{d(\hat{\mathbf{b}}, \mathbf{b}^{(1)})}{d(\hat{\mathbf{b}}, \mathbf{b}^{(2)})} = \frac{d(\hat{\mathbf{x}}_{\text{corr}}^{n+1}, \mathbf{x}^{(1)})}{d(\hat{\mathbf{x}}_{\text{corr}}^{n+1}, \mathbf{x}^{(2)})}. \quad (45)$$

This is achieved by computing $\hat{\mathbf{x}}_{\text{corr}}^{n+1}$ as

$$\hat{\mathbf{x}}_{\text{corr}}^{n+1} = \frac{d_{\mathbf{b}}^{(2)} \mathbf{x}^{(1)} + d_{\mathbf{b}}^{(1)} \mathbf{x}^{(2)}}{d_{\mathbf{b}}^{(1)} + d_{\mathbf{b}}^{(2)}}, \quad (46)$$

where $d_{\mathbf{b}}^{(i)} = d(\hat{\mathbf{b}}, \mathbf{b}^{(i)})$ is given by (40).

In addition to the two CNM parameters (number of centroids K and model order L), CNMc requires three more settings: The number of closest centroids in each neighboring test case, the norm for the nearest neighbor distance and the optional position correction. These parameters can be optimized for each application separately. One possible approach to optimize these parameters is the hold-out method, where the RMSE is evaluated on the autocorrelation functions.

Table 3: CNMc settings for the Lorenz system and boundary layer applications.

Application	Number of clusters K	Model order L	Number of neighboring centroids	Distance norm	Position correction
Lorenz system	250	83	1	Euclidean	No
Boundary layer	120	15	3	L_{10}	Yes

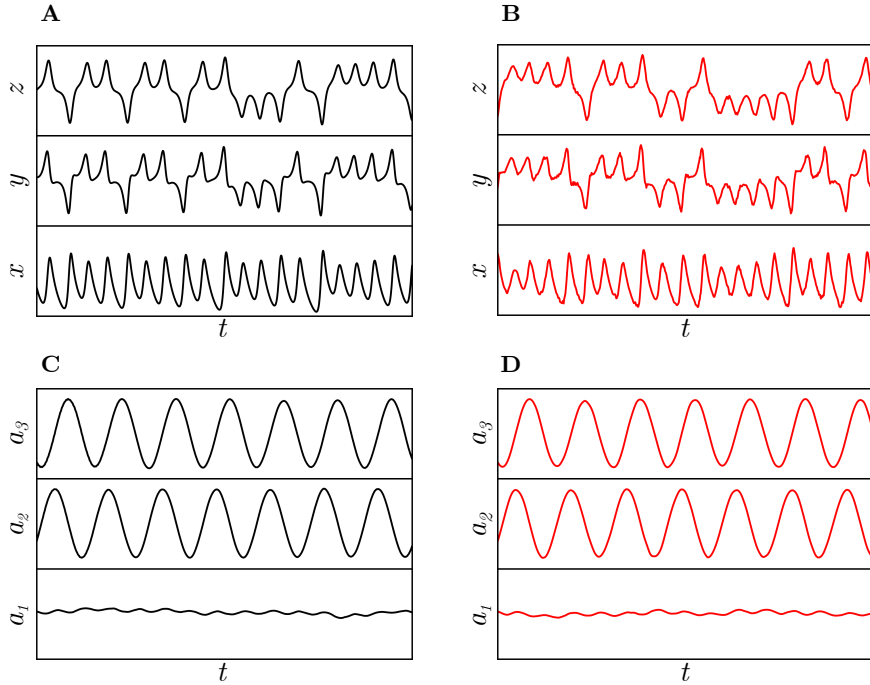


Fig. 14. Time series modeling with CNMc. Time series of the reference data (black) and the predicted cases (red) for the (A) (B) the Lorenz system and the (C) (D) actuated turbulent boundary layer. The Lorenz attractor with $\rho = 28$ is interpolated from two test cases with $\rho = 26$ and $\rho = 30$ and the boundary layer with actuation parameters $\lambda^+ = 1000$, $T^+ = 120$ and $A^+ = 30$ is interpolated from cases with $\lambda^+ = 1000$, $T^+ = 120$, $A^+ = 20$, and $\lambda^+ = 1000$, $T^+ = 120$ and $A^+ = 40$. For both applications, the main dynamical features are well reconstructed.

The CNMc parameters for the interpolated Lorenz system and for the boundary layer are summarized in Table 3. The corresponding time series for these two applications are presented in Fig. 14.

Algorithm 1: CNMc procedure

Extract the centroids of the two closest test cases;
Initialize the state $\hat{\mathbf{x}}^{n=0} = \hat{\mathbf{x}}^0$;
Time initialization $t^{n=0} = t^0 = 0$;
while $t^n < T_{max}$ **do**
 for $i \leftarrow 1, 2$ **do**
 Find the N_k nearest centroids from test case (i) : $\mathbf{c}_{n_k}^{(i),n}$, $n_k = 1, \dots, N_k$;
 for $n_k \leftarrow 1$ **to** N_k **do**
 Identify past trajectory of $\mathbf{c}_{n_k}^{(i),n}$;
 Get transition time $T_{n_k}^{(i)}$;
 Get next centroid $\mathbf{c}_{n_k, \text{next}}^{(i)}$ and transition vector $\mathbf{v}_{n_k}^{(i)} = \mathbf{c}_{n_k}^{(i),n+1} - \mathbf{c}_{n_k}^{(i),n}$;
 end
 end
 Average transition time $\hat{T} = \frac{1}{2N_k} \sum_{i=1}^2 \sum_{n_k=1}^{N_k} T_{n_k}^{(i)}$;
 Average transition vector $\hat{\mathbf{v}} = \frac{1}{2N_k} \sum_{i=1}^2 \sum_{n_k=1}^{N_k} \mathbf{v}_{n_k}^{(i)}$;
 Update position $\hat{\mathbf{x}}^{n+1} = \hat{\mathbf{x}}^n + \hat{\mathbf{v}}$;
 Correct position $\hat{\mathbf{x}}_{\text{corr}}^{n+1}$;
 Update time $t^{n+1} = t^n + \hat{T}$;
 Update iteration number $n = n + 1$
end

References

- [1] P. Holmes, J. L. Lumley, G. Berkooz, C. W. Rowley, *Turbulence, coherent structures, dynamical systems and symmetry* (Cambridge university press, 2012).
- [2] P. Benner, S. Gugercin, K. Willcox, A survey of projection-based model reduction methods for parametric dynamical systems. *SIAM Review* **57**, 483–531 (2015).
- [3] J. H. Tu, C. W. Rowley, D. M. Luchtenburg, S. L. Brunton, J. N. Kutz, On dynamic mode decomposition: Theory and applications. *Journal of Computational Dynamics* **1**, 391 (2014).
- [4] H. Ye, R. J. Beamish, S. M. Glaser, S. C. Grant, C.-h. Hsieh, L. J. Richards, J. T. Schnute, G. Sugihara, Equation-free mechanistic ecosystem forecasting using empirical dynamic modeling. *Proceedings of the National Academy of Sciences* **112**, E1569–E1576 (2015).
- [5] S. L. Brunton, B. R. Noack, P. Koumoutsakos, Machine learning for fluid mechanics. *Ann. Rev. Fluid Mech.* **52**, 477–508 (2020).

- [6] J. Bongard, H. Lipson, Automated reverse engineering of nonlinear dynamical systems. *Proceedings of the National Academy of Sciences* **104**, 9943–9948 (2007).
- [7] M. Schmidt, H. Lipson, Distilling Free-Form Natural Laws from Experimental Data. *Science* **324**, 81–85 (2009).
- [8] S. L. Brunton, J. L. Proctor, J. N. Kutz, Discovering governing equations from data by sparse identification of nonlinear dynamical systems. *Proceedings of the national academy of sciences* **113**, 3932–3937 (2016).
- [9] F. C. Fu, J. B. Farison, On the Volterra series functional evaluation of the response of non-linear discrete-time systems. *International Journal of Control* **18**, 553–558 (1973).
- [10] C. Chatfield, *Time-series forecasting* (CRC press, 2000).
- [11] J.-N. Juang, *Applied system identification* (Prentice-Hall, Inc., 1994).
- [12] T. Wang, H. Gao, J. Qiu, A combined adaptive neural network and nonlinear model predictive control for multirate networked industrial process control. *IEEE Transactions on Neural Networks and Learning Systems* **27**, 416–425 (2016).
- [13] M. Newman, The physics of networks. *Physics today* **61**, 33–38 (2008).
- [14] A.-L. Barabási, R. Albert, Emergence of scaling in random networks. *Science* **286**, 509–512 (1999).
- [15] A.-L. Barabási, E. Bonabeau, Scale-free networks. *Scientific American* **288**, 60–69 (2003).
- [16] J. R. Norris, *Markov chains*, no. 2 (Cambridge university press, 1998).
- [17] N. Marwan, J. F. Donges, Y. Zou, R. V. Donner, J. Kurths, Complex network approach for recurrence analysis of time series. *Physics Letters A* **373**, 4246–4254 (2009).
- [18] K. Taira, A. G. Nair, S. L. Brunton, Network structure of two-dimensional decaying isotropic turbulence. *Journal of Fluid Mechanics* **795** (2016).
- [19] E. Kaiser, B. R. Noack, L. Cordier, A. Spohn, M. Segond, M. Abel, G. Daviller, J. Östh, S. Krajnović, R. K. Niven, Cluster-based reduced-order modelling of a mixing layer. *Journal of Fluid Mechanics* **754**, 365–414 (2014).
- [20] H. Li, D. Fernex, R. Semaan, J. Tan, M. Morzyński, B. R. Noack, Cluster-based network model. *Journal of Fluid Mechanics* (in print), see arXiv:2001.02911 (2020).
- [21] W.-K. Ching, X. Huang, M. K. Ng, T.-K. Siu, *Markov Chains: Models, Algorithms and Applications*, International Series in Operations Research & Management Science (Springer, 2013), pp. 141–176.

- [22] B. C. Daniels, I. Nemenman, Automated adaptive inference of phenomenological dynamical models. *Nature Communications* **6**, 8133 (2015).
- [23] D. Arthur, S. Vassilvitskii, k-means++: The advantages of careful seeding, *Tech. rep.*, Stanford (2006).
- [24] A. K. Jain, M. N. Murty, P. J. Flynn, Data clustering: a review. *ACM Computing Surveys* **31**, 264–323 (1999).
- [25] F. Takens, *Dynamical systems and turbulence, Warwick 1980*, Lecture Notes in Mathematics (Springer, University of Warwick, 1981), pp. 366–381.
- [26] E. N. Lorenz, Deterministic Nonperiodic Flow. *Journal of the Atmospheric Sciences* **20**, 130–141 (1963).
- [27] B. Protas, B. R. Noack, J. Östh, Optimal nonlinear eddy viscosity in Galerkin models of turbulent flows. *Journal of Fluid Mechanics* **766**, 337–367 (2015).
- [28] O. E. Rössler, An equation for continuous chaos. *Physics Letters A* **57**, 397–398 (1976).
- [29] S. L. Brunton, B. W. Brunton, J. L. Proctor, E. Kaiser, J. N. Kutz, Chaos as an intermittently forced linear system. *Nature Communications* **8**, 19 (2017).
- [30] M. Farazmand, T. P. Sapsis, A variational approach to probing extreme events in turbulent dynamical systems. *Science Advances* **3**, e1701533 (2017).
- [31] M. Albers, P. S. Meysonnat, D. Fernex, R. Semaan, B. R. Noack, W. Schröder, Drag Reduction and Energy Saving by Spanwise Traveling Transversal Surface Waves for Flat Plate Flow. *Flow, Turbulence and Combustion* **105**, 125–157 (2020).
- [32] Z. Y. Wan, P. Vlachas, P. Koumoutsakos, T. Sapsis, Data-assisted reduced-order modeling of extreme events in complex dynamical systems. *PLOS ONE* **13**, e0197704 (2018).
- [33] G. Van Rossum, F. L. Drake, *The python language reference manual* (Network Theory Ltd., 2011).
- [34] P. Virtanen, R. Gommers, T. E. Oliphant, M. Haberland, T. Reddy, D. Cournapeau, E. Burovski, P. Peterson, W. Weckesser, J. Bright, S. J. van der Walt, M. Brett, J. Wilson, K. J. Millman, N. Mayorov, A. R. J. Nelson, E. Jones, R. Kern, E. Larson, C. J. Carey, I. Polat, Y. Feng, E. W. Moore, J. VanderPlas, D. Laxalde, J. Perktold, R. Cimrman, I. Henriksen, E. A. Quintero, C. R. Harris, A. M. Archibald, A. H. Ribeiro, F. Pedregosa, P. van Mulbregt, SciPy 1.0: fundamental algorithms for scientific computing in Python. *Nature Methods* **17**, 261–272 (2020).

- [35] A. L. Goldberger, L. A. Amaral, L. Glass, J. M. Hausdorff, P. C. Ivanov, R. G. Mark, J. E. Mietus, G. B. Moody, C. K. Peng, H. E. Stanley, PhysioBank, PhysioToolkit, and PhysioNet: components of a new research resource for complex physiologic signals. *Circulation* **101**, 215–220 (2000).
- [36] E. D. Fylladitakis, Kolmogorov Flow: Seven Decades of History. *Journal of Applied Mathematics and Physics* **6**, 2227–2263 (2018).
- [37] M. Farazmand, T. P. Sapsis, Dynamical indicators for the prediction of bursting phenomena in high-dimensional systems. *Physical Review E* **94**, 032212 (2016).
- [38] D. Bechert, W. Reif, *23rd Aerospace Sciences Meeting* (American Institute of Aeronautics and Astronautics, 1985), p. 546.
- [39] M. Luhar, A. S. Sharma, B. J. McKeon, On the design of optimal compliant walls for turbulence control. *Journal of Turbulence* **17**, 787–806 (2016).
- [40] Y. Du, G. E. Karniadakis, Suppressing wall turbulence by means of a transverse traveling wave. *Science* **288**, 1230–1234 (2000).
- [41] M. Quadrio, Drag reduction in turbulent boundary layers by in-plane wall motion. *Philosophical Transactions of the Royal Society A: Mathematical, Physical and Engineering Sciences* **369**, 1428–1442 (2011).
- [42] D. Fernex, R. Semaan, M. Albers, P. S. Meysonnat, W. Schröder, B. R. Noack, Actuation response model from sparse data for wall turbulence drag reduction. *Physical Review Fluids* **5**, 073901 (2020).
- [43] J. MacQueen (University of California, 1967), vol. 1. Conference Name: Proceedings of the Fifth Berkeley Symposium on Mathematical Statistics and Probability.
- [44] S. Lloyd, Least squares quantization in PCM. *IEEE Transactions on Information Theory* **28**, 129–137 (1982). Conference Name: IEEE Transactions on Information Theory.
- [45] D. Fernex, R. Semaan, M. Albers, P. S. Meysonnat, W. Schröder, R. Ishar, E. Kaiser, B. R. Noack, Cluster-based network model for drag reduction mechanisms of an actuated turbulent boundary layer. *Proceedings in Applied Mathematics and Mechanics* **19** (2019).
- [46] Y. Cao, E. Kaiser, J. Borée, B. R. Noack, L. Thomas, S. Guilain, Cluster-based analysis of cycle-to-cycle variations: application to internal combustion engines. *Experiments in Fluids* **55**, 1837 (2014).
- [47] R. Ishar, E. Kaiser, M. Morzyński, D. Fernex, R. Semaan, M. Albers, P. S. Meysonnat, W. Schröder, B. R. Noack, Metric for attractor overlap. *Journal of Fluid Mechanics* **874**, 720–755 (2019).

- [48] J. Östh, E. Kaiser, S. Krajnović, B. R. Noack, Cluster-based reduced-order modelling of the flow in the wake of a high speed train. *Journal of Wind Engineering and Industrial Aerodynamics* **145**, 327–338 (2015).
- [49] J. L. Bentley, Multidimensional binary search trees used for associative searching. *Communications of the ACM* **18**, 509–517 (1975).